UNIVERSITY OF CALIFORNIA SAN DIEGO

Wearable ultrasound systems for operator-free healthcare monitoring

A Dissertation submitted in partial satisfaction of the requirements
for the degree Doctor of Philosophy

in

Nanoengineering

by

Muyang Lin

Committee in charge:

Professor Sheng Xu, Chair
Professor Jinhye Bae
Professor Gert Cauwenberghs
Professor Joseph Wang

2024

The Dissertation of Muyang Lin is approved, and it is acceptable in quality and form for publication on microfilm and electronically.

University of California San Diego

2024

DEDICATION

This dissertation marks not only a milestone in my academic career but also a significant chapter in my personal journey. It is a testament to the collective effort, unwavering support, and endless encouragement I have received from many.

First and foremost, I extend my deepest gratitude to my advisor, Prof. Sheng Xu. His guidance has been invaluable. Prof. Xu's expertise, patience, and insightful feedback have not only shaped my research but also fostered my academic growth. His mentorship extends beyond the realms of academia, imparting lessons that resonate deeply in all aspects of my life.

To my family, my unwavering foundation and constant source of support: Your unconditional love, endless patience, and belief in my abilities have propelled me forward in every endeavor. The sacrifices you've made and your steadfast support have made this journey not only possible but meaningful. For this, I am eternally grateful.

I am also indebted to my peers, particularly C. Wang, my first and exemplary mentor who guided me onto the path of research. To my lab colleagues Y. Bian, S. Qin, X. Chen, S. Zhou, and many others: Your collaboration and shared wisdom have immensely enriched my experience and significantly contributed to my research. My friends J. Zhou, S. Shen, and Z. Hui, have also been pillars of support, offering camaraderie and comfort during this journey.

Lastly, special thanks to my fluffy friend, Toby the cat, whose companionship and amusing antics have provided delightful respite and joy throughout this challenging yet rewarding journey.

To each one of you, I dedicate this work with my deepest appreciation and heartfelt thanks.

TABLE OF CONTENTS

LIST OF FIGURES

LIST OF TABLES

ACKNOWLEDGEMENTS

I would like to acknowledge Professor Sheng Xu for his support as the chair of my committee. Through multiple drafts and many long nights, his guidance has proved to be invaluable.

Chapter 1-4, in full, is a reprint of the material as it appears in Nature Biotechnology. Muyang Lin, Ziyang Zhang, Xiaoxiang Gao, Yizhou Bian, Ray S. Wu, Geonho Park, Zhiyuan Lou, Zhuorui Zhang, Xiangchen Xu, Xiangjun Chen, Andrea Kang, Xinyi Yang, Wentong Yue, Lu Yin, Chonghe Wang, Baiyan Qi, Sai Zhou, Hongjie Hu, Hao Huang, Mohan Li, Yue Gu, Jing Mu, Albert Yang, Amer Yaghi, Yimu Chen, Yusheng Lei, Chengchangfeng Lu, Ruotao Wang, Joseph Wang, Shu Xiang, Erik B. Kistler, Nuno Vasconcelos & Sheng Xu. "A fully integrated wearable ultrasound system to monitor deep tissues in moving subjects." Nature Biotechnology, 2023. The dissertation author was the primary investigator and author of this paper.

Chapter 5, in part, is a reprint of the material as it appears in Nature Biotechnology. Muyang Lin, Ziyang Zhang, Xiaoxiang Gao, Yizhou Bian, Ray S. Wu, Geonho Park, Zhiyuan Lou, Zhuorui Zhang, Xiangchen Xu, Xiangjun Chen, Andrea Kang, Xinyi Yang, Wentong Yue, Lu Yin, Chonghe Wang, Baiyan Qi, Sai Zhou, Hongjie Hu, Hao Huang, Mohan Li, Yue Gu, Jing Mu, Albert Yang, Amer Yaghi, Yimu Chen, Yusheng Lei, Chengchangfeng Lu, Ruotao Wang, Joseph Wang, Shu Xiang, Erik B. Kistler, Nuno Vasconcelos & Sheng Xu. "A fully integrated wearable ultrasound system to monitor deep tissues in moving subjects." Nature Biotechnology, 2023. The dissertation author was the primary investigator and author of this paper.

VITA

2018 Bachelor of Engineering in Measurement and Control Technology and Instrument, Tianjin University

2019 Master of Science in Nanoengineering, University of California San Diego

2024 Doctor of Philosophy in Nanoengineering, University of California San Diego

PUBLICATIONS

1. Lin, M., Zhang Z., Gao X., et al. A fully integrated wearable ultrasound system to monitor deep tissues in moving subjects. Nat. Biotechnol., 1-10 (2023).
2. Lin, M., Hu, H., Zhou, S. & Xu, S. Soft wearable devices for deep-tissue sensing. Nat. Rev. Mater. 7, 850–869 (2022).
3. Sempionatto, J. R., Lin, M. (co-first), et al. An epidermal patch for the simultaneous monitoring of haemodynamic and metabolic biomarkers. Nat. Biomed. Eng. 5, 737-748 (2021).
4. Wang C., Qi B., Lin M. (co-first), et al. Continuous monitoring of deep-tissue haemodynamics with stretchable ultrasonic phased arrays. Nat. Biomed. Eng. 5, 749-758 (2021).
5. Lin, M., et al. Soft sensors form a network. Nat. Electron. 2, 327-328 (2019).
6. Huang, H., Wu, R., Lin M. (co-first), et al. Emerging Wearable Ultrasound Technology.IEEE Transactions on Ultrasonics, Ferroelectrics, and Frequency Control (2023).
7. Xu, Y., De la Paz, E., … Lin M., et al. In-ear integrated sensor array for the continuous monitoring of brain activity and of lactate in sweat. Nat. Biomed. Eng 7.10 (2023): 1307-1320.
8. Wang C., Li X., Hu H., … Lin M., et al. Monitoring of the central blood pressure waveform via conformal ultrasonic device. Nat. Biomed. Eng. 2, 687-695 (2018).
9. Hu H., Huang H., Li M., … Lin M, et al. A wearable cardiac ultrasound imager. Nature 613, 667-675 (2023).
10. Hu H., Ma Y., Gao X., … Lin M, et al. Stretchable ultrasonic arrays for the three-dimensional mapping of the modulus of deep tissue. Nat. Biomed. Eng. (2023)
11. Gao X., Chen X., Hu H., … Lin M, et al. A photoacoustic patch for three-dimensional imaging of hemoglobin and core temperature. Nat. Commun. 13, 7757 (2022).
12. Gu Y., Wang C., Kim N., … Lin M, et al. Three-dimensional transistor arrays for intra- and inter-cellular recording. Nat. Nanotechnol. 17, 292-300 (2022).
13. Yin L., Cao M., Kim K N., … Lin M, et al. A stretchable epidermal sweat sensing platform with an integrated printed battery and electrochromic display. Nat. Electron. 5, 694-705 (2022).
14. Yin L., Kim K N., Lv J., … Lin M, et al. A self-sustainable wearable multi-modular E-textile bioenergy microgrid system. Nat. Commun. 12, 1-12 (2021).
15. Chen X., Gao X., Nomoto A., … Lin M, et al. Fabric-substrated capacitive biopotential sensors enhanced by dielectric nanoparticles. Nano Res., 1-5 (2021).

FIELD OF STUDY

Major Field: Biomedical engineering

Studies in wearable electronics

Professor Sheng Xu

ABSTRACT OF THE DISSERTATION

Wearable ultrasound systems for operator-free healthcare monitoring

by

Muyang Lin

Doctor of Philosophy in Nanoengineering

University of California San Diego, 2024

Professor Sheng Xu, Chair

Medical ultrasound is a powerful tool for diagnosis. However, conventional ultrasound devices suffer from operator dependency and do not allow long-term usage. Recent advances in wearable ultrasound technologies have demonstrated the potential for hands-free data acquisition, but technical barriers remain as these probes require wire connections, can lose track of moving targets, and create data-interpretation challenges. Here, I report a fully

integrated autonomous wearable ultrasonic-system-on-patch (USoP). A miniaturized flexible control circuit is designed to interface with an ultrasound transducer array for signal pre-conditioning and wireless data communication. Machine learning is used to track moving tissue targets and assist the data interpretation. I demonstrate that the USoP allows continuous tracking of physiological signals from tissues as deep as 164 mm. On mobile subjects, the USoP can continuously monitor physiological signals, including central blood pressure, heart rate, and cardiac output, for as long as two hours. This result enables continuous autonomous surveillance of deep tissue signals toward internet-of-medical-things.

INTRODUCTION

With decades of development in probe fabrication[1,2], circuitry design[3], and algorithm optimization[4,5], medical ultrasonography[6] can qualitatively and quantitatively acquire a broad range of physiological information from the human body[7,8], including anatomical structures[9], tissue motion[10], mechanical properties[11], and haemodynamics[12]. Compared with other medical imaging methods[13], such as X-ray computed tomography[14] and magnetic resonance imaging[15], ultrasonography is safer, less expensive, and more versatile. However, the accessibility and accuracy of ultrasonography face several technical challenges. First, common ultrasound probes are bulky and wired to large control systems, which limits their usage to centralized facilities. Second, those probes need manual placement and maneuvering and require the subjects to remain motionless, introducing operator-dependency. Third, the interpretation of sonographic data requires medical professionals with specialized training and is labor-intensive and error-prone.

Recent advances in point-of-care ultrasound systems[16] have substantially reduced the device size. However, they either need manual operations[3], or require bulky rigid circuits[17] because ultrasound hardware typically requires high power and high bandwidth. The use of bulky rigid probes and circuits create difficulties to cover a large area and conform to highly-curved body surfaces. Emerging wearable ultrasonic probes leveraging soft structural designs can naturally conform to the skin and acquire deep tissue signals in a hands-free manner[18-20]. Alternatively, integrating rigid ultrasound chips with soft adhesive materials can achieve a reliable interface on the human skin[21]. However, these wearable probes all require cumbersome cables for power and data transmission[3,21], which substantially limits the subjects' mobility, making surveillance challenging during dynamic tests or normal daily activities. Developing a fully integrated

ultrasonic probe with soft front-end circuits has yet to be demonstrated[22,23]. Additionally, current wearable ultrasound technologies can lose track of a target tissue during subject motion, because the device on the skin surface shifts its position relative to deep tissues. Thus, they require frequent manual repositioning and only allow point-in-time examinations[3,24]. Moreover, with the large amount of data generated from continuous surveillance, the front-end circuits and back-end processing units would be overwhelmed. Therefore, a critical milestone in the development of wearable ultrasound technology is to realize a fully integrated wireless system that can track a moving target and automate data acquisition and processing.

Here, I report a fully integrated autonomous ultrasonic-system-on-patch (USoP). The USoP integrates the ultrasonic probe and miniaturized wireless control electronics in a soft, wearable format, which overcomes the above-mentioned limitations. Multiple channels of deep tissue signals acquired from the subject are conditioned and preprocessed on-board, then wirelessly transferred to a backend receiver, where they are analyzed by a customized machine learning algorithm. When the USoP on the skin moves relative to the target tissue, the algorithm classifies the data and selects the best channel in real time, yielding a continuous data stream from the target tissue. Therefore, this technology allows continuous monitoring of deep tissue signals during human motion. The fully integrated autonomous USoP eliminates the operator dependency of conventional ultrasonography, standardizes the data interpretation process, and therefore expands the accessibility of this powerful diagnostic tool in both inpatient and outpatient settings.

Chapter 1 Design of the hardware system

The USoP hardware consists of an ultrasound probe and control electronics which are fabricated in a miniaturized, soft format (Fig. 1.1a). The ultrasonic probe is made of piezoelectric transducers, backing materials, serpentine interconnects, and contact pads, similar to previously reported structures[19,20,25]. This soft probe design reduced noise coupling by isolating the signal line from the skin surface (Fig. 1.2). A silicone elastomer with a low modulus of 69 kPa is used for the probe-skin interface, which ensured intimate contact between the transducers and skin, therefore enable gel-free acoustic sensing[19] (Fig. 1.3).

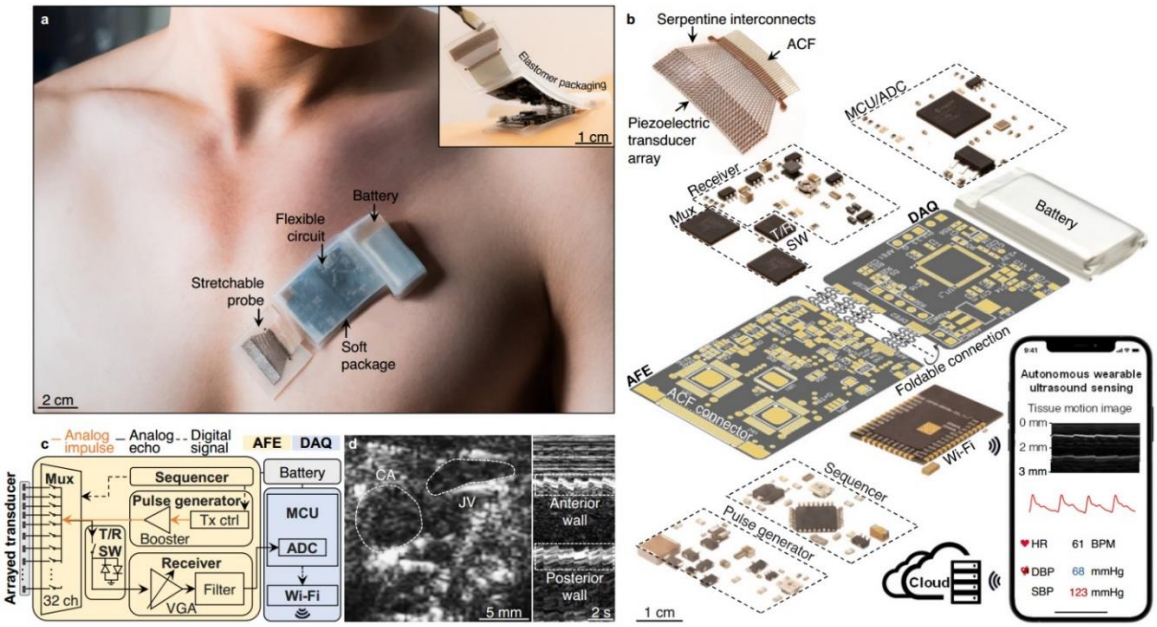

Figure 1.1: Overview of the fully integrated USoP. a, A photo of the encapsulated USoP worn on the chest. The inset shows the folded USoP. b, Design of the USoP, including a stretchable ultrasonic probe, a flexible control circuit, and a battery. The ultrasonic probe consists of a piezoelectric transducer array, serpentine interconnects, and an anisotropic conductive film (ACF) (upper left). The exploded view of the circuit shows two parts: an AFE and a DAQ module. The two modules are connected by serpentine electrodes, which allow the entire circuit to be folded for a smaller footprint. A smartphone application is designed to host the data stream from the USoP. The smartphone can also serve as a relay to transmit the data to a cloud server for further analysis (lower right). c, Block diagram of the USoP showing the flow of analog impulse, analog echo, and digital signals. The AFE senses pulse-echo to generate ultrasonic signals, and the DAQ samples signals and wirelessly transmits the data to a smartphone for processing and display. d, B-mode imaging of the carotid artery (CA) and jugular vein (JV), while the subject is performing the Valsalva maneuver to dilate the JV (left). M-mode imaging of the pulsation pattern of CA walls (right).

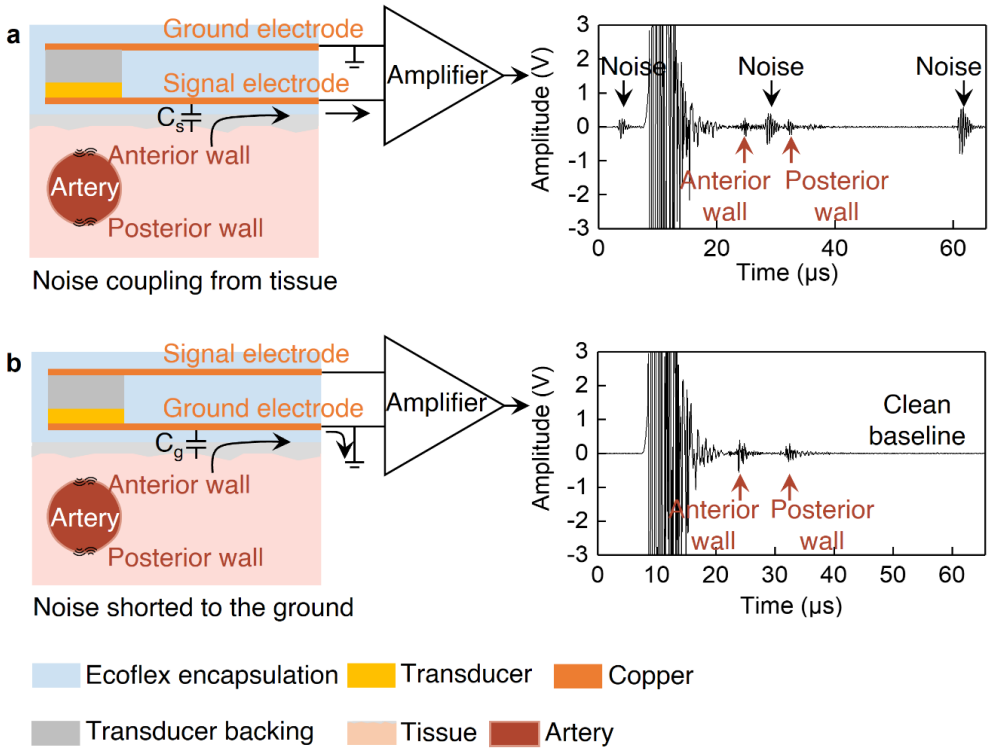

Figure 1.2: Probe layout designs for reducing noise coupling. a, When the signal electrode faces the skin, the parasitic capacitor Cs can directly conduct the in-band noise to the amplifier, resulting in a high noise floor. b, When the ground electrode faces the skin, the capacitor Cg will short the noise signals to the ground without interfering with the signal line. As a result, the received radiofrequency signal will have a cleaner baseline.

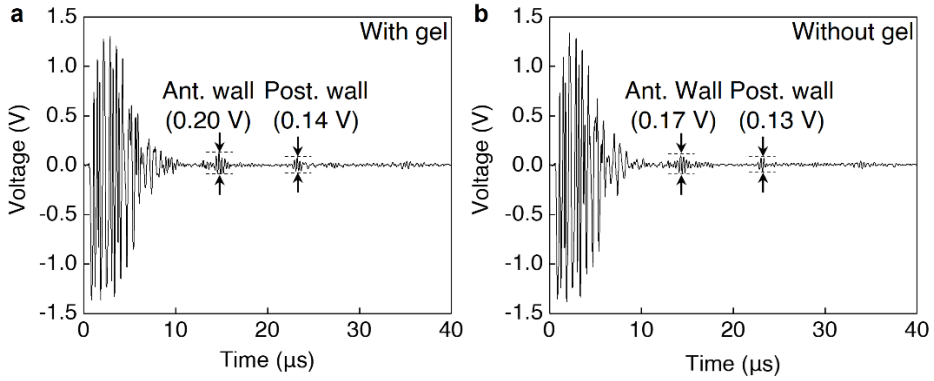

Figure 1.3: Radiofrequency signals collected from the carotid artery with and without gel. The arterial wall echoes acquired with gel (a) and without gel (b) were both strong and distinguishable. The results showed the echo amplitude would decrease by less than 15% when the gel was not applied. Therefore, gel-free measurements experience minimal signal degradation.

The probes are degisned with center frequencies from 2 MHz to 6 MHz to achieve the desired bandwidth, axial resolution, and penetration. The bandwidth is determined as the -3 dB frequency band of the pulse-echo response, spatial resolution as the full width at half maximum of the pulse-echo response, and penetration depth as the -3 dB attenuation point in tissues. All soft probes can achieve a relative bandwidth of ~50%, which is similar to a commercial probe (Fig. 1.4). The 2 MHz transducers achieve a depth of ~164 mm with an axial resolution of ~600 μm for targeting visceral organs (e.g., heart and diaphragm). The 4 MHz transducers achieve a depth of ~78 mm with an axial resolution of ~330 μm for targeting major arteries (e.g., aorta, carotid, and femoral arteries). The 6 MHz transducers achieve a depth of ~9 mm and an axial resolution of ~230 μm for targeting smaller peripheral arteries (e.g., radial and brachial arteries). To achieve desired beam profiles, three probe layouts are customized: disc, linear array, and two-dimensional array, for penetrative, wide, and narrow beam, respectively (Fig. 1.5).

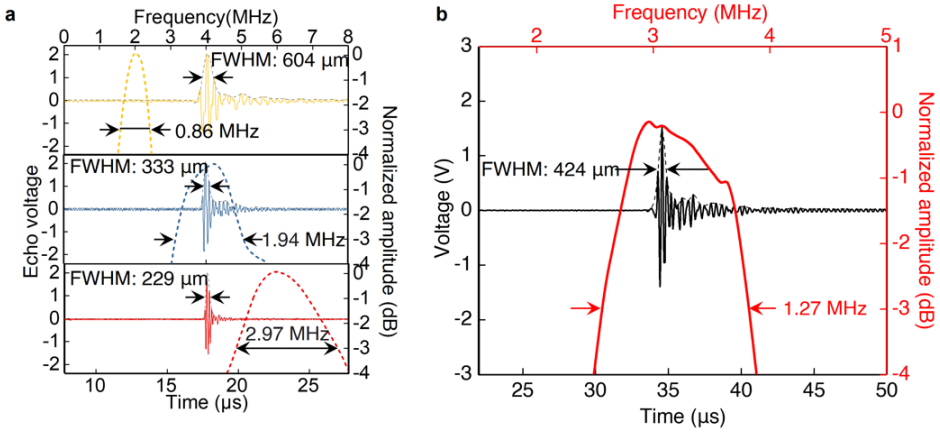

Figure 1.4: Characterizing bandwidth, axial resolution, and penetration of the stretchable ultrasonic probes. a, Pulse-echo response and bandwidth of the probes with three frequencies. The full width at half maximum (FWHM) is labeled to show the axial resolution of each probe. The 2 MHz, 4 MHz, and 6 MHz can achieve 604 μm, 333 μm, and 229 μm resolution, respectively. Three probes could achieve a relative bandwidth of ~50% to their center frequencies at -3 dB. b, The pulse-echo response of a commercial ultrasound probe with a center frequency of 3 MHz, which could achieve a relative bandwidth of 42.3%.

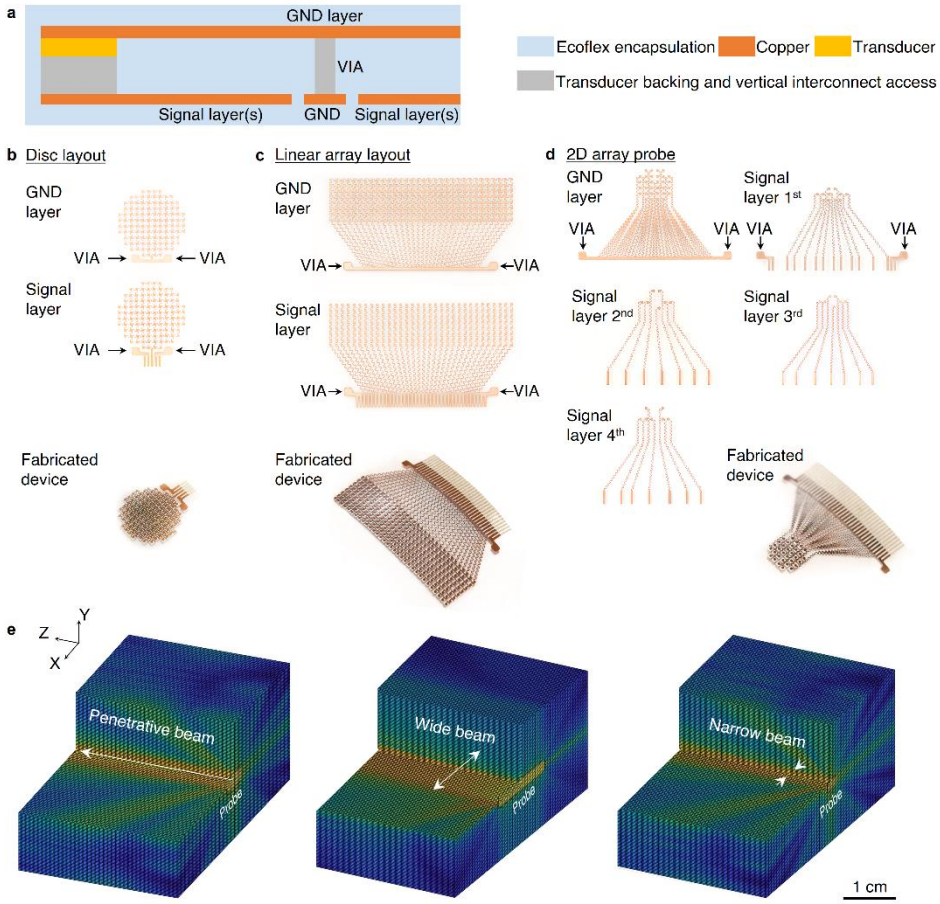

Figure 1.5: Layout and beam profile designs of three soft probes. a, A cross-sectional view of the stretchable probe design. The transducer and the backing layer are sandwiched by two layers of electrodes (ground (GND) and signal layers). A vertical interconnect access (VIA) is used to lead the ground electrode to the signal layer for connection. b, The two electrodes for the disc probe. The electrodes connect 112 transducers in parallel. c, The two electrodes for the linear array probe. The signal layer consists of 32 channels, and each channel has 8 pixels connected in parallel. d, The two electrodes for the 2D array probe. 32 transducers are grounded by one bottom electrode. The signal layer is distributed into four layers. e, Simulated acoustic transmission fields of the three probe designs, where penetrative, wide, and narrow beam profiles could be achieved by the disc, linear array, and 2D layouts, respectively.

The three probe layout designs (i.e., a disc, a linear array, and a 2D array) (Fig. 1.5). were simulated to confirm their transmission characteristics, where distinct beam patterns and aperture coverages were illustrated (Fig. 1.5e). For the disc, 112 piezoelectric transducers at 2 MHz were used. All of these transducers were arranged within a circular region and connected in parallel, functioning as a single transducer for high transmission intensity. Such a design resulted in a highly

penetrative transmission beam (Fig. 1.5e left), which was suitable for sensing deep organs (e.g., heart and diaphragm). For the linear array, 256 transducers at 4 MHz were arranged with a bi-axial pitch of 0.8 mm. 8 transducers in the same column were connected in parallel to enhance the transmission intensity. 32 such columns constituted the linear array, yielding a 25.4 mm ultrasonographic aperture at moderate penetration depth (Fig. 1.5e middle), which was suitable for sensing central arteries (e.g., carotid artery, femoral artery, and abdominal aorta). For the 2D array, 32 transducers at 6 MHz were used to constitute the array with a 0.8 mm bi-axial pitch. The overall dimension of the 2D array was the smallest in comparison with the other two cases. Such a design guaranteed a narrow beam (Fig. 1.5e right), which allowed for high spatial resolution sensing for shallow (e.g., radial and brachial) arteries.

Besides the soft probe design, the control electronics play an critical role in ultrasonic sensing. The control electronics are designed as a flexible printed circuit board (Fig. 1.6 and Table 1.1**)** for ultrasonic sensing and wireless communication. The circuitry consists of an analog front-end (AFE) and a data acquisition (DAQ) module (Fig. 1.1b). The AFE achieves ultrasonic sensing through coordinated sequence control of multiple components (Fig. 1.7). First, the sequencer initiates sensing by sending trigger signals to the pulse generator and multiplexer. Then, the pulse generator reads the trigger signals and outputs high-voltage impulses to activate the ultrasound transducers. Meanwhile, the multiplexer drives the arrayed transducers to generate ultrasound and receive echoes. Finally, the echoes are collected by the transmit/receive switch, and then amplified and filtered by the receiver circuit. After the AFE completes the ultrasonic sensing process, the analog echoes are relayed to the DAQ module. The microcontroller unit (MCU) samples the echoes with a built-in analog-to-digital converter, and then the Wi-Fi module wirelessly transmits

the digitalized echoes to a terminal device (e.g., a smartphone), where an online machine learning algorithm and an application program can process and display the signals autonomously (Fig. 1.1c).

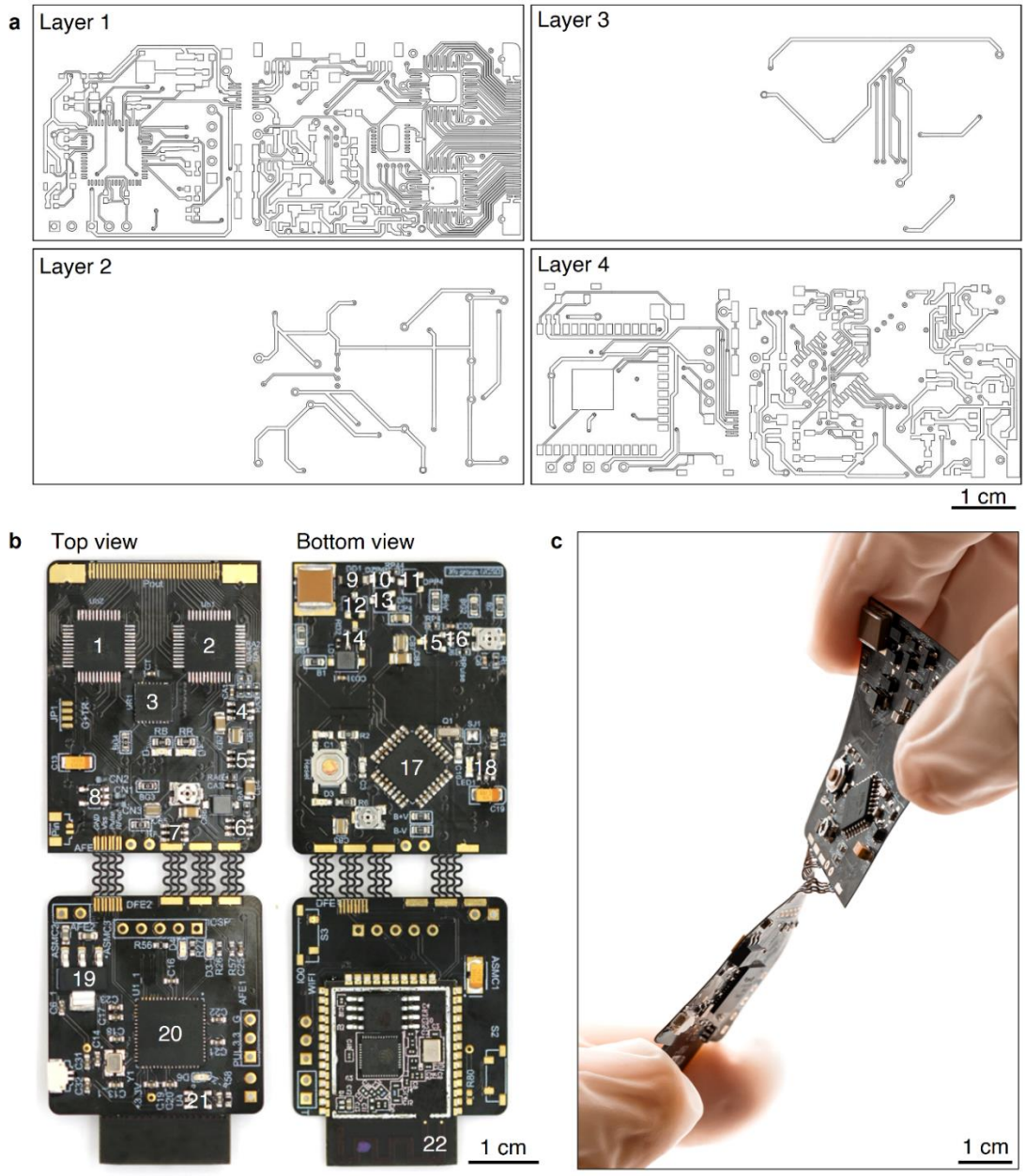

Figure 1.6: Layout designs of the fPCB circuit. a, Layouts of the fPCB with four layers of interconnects. b, Photos of the fPCB with key components (Table 1.1) labeled. The analog front-end is 3 cm × 4 cm in size. The wireless data acquisition module is 3 cm × 3 cm in size. **c**, The circuit being bent and twisted to show its flexibility.

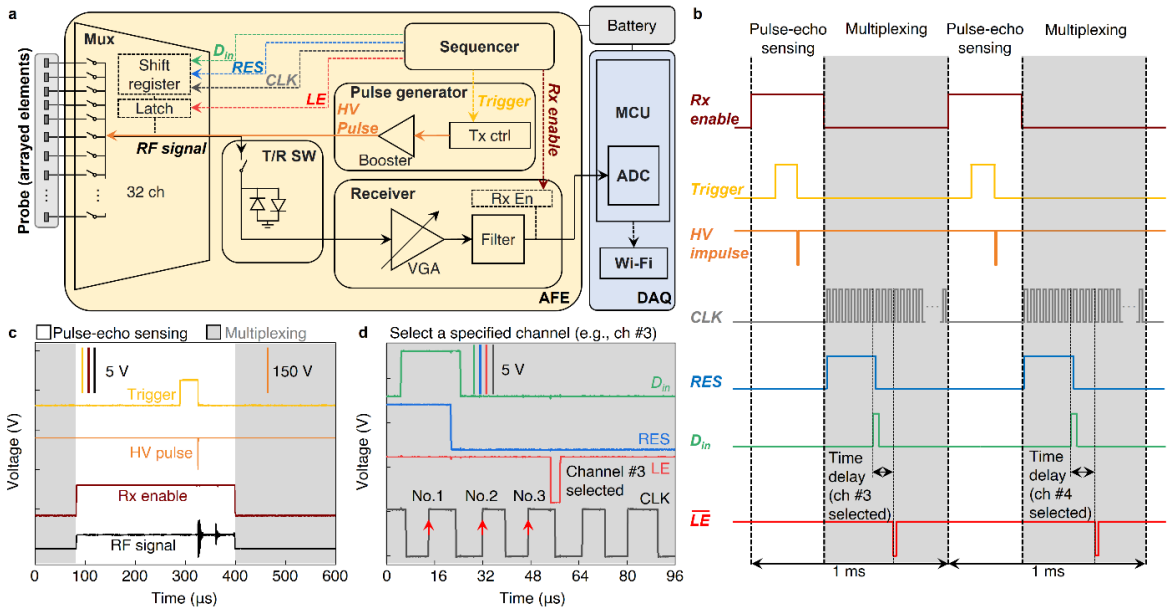

Figure 1.7: Schematics and control sequence of ultrasonic sensing. a, Block diagram and signal transmission lines between the functional modules. The control circuit includes two functional parts: the AFE and the wireless DAQ module. The AFE consists of a multiplexer (Mux), a transmit/receive switch (T/R SW), a receiver, a sequencer, and a pulse generator. The DAQ module consists of a microcontroller (MCU) with on-chip analog-to-digital convertor (ADC), and a Wi-Fi transmitter. The dashed lines are for digital signal transmission and the solid lines are for analog signal transmission. b, The simulated control sequence for multiplexing and pulse-echo sensing, which shows the time sequence of the receive (Rx) enable, trigger, high-voltage (HV) pulse, clock (CLK), reset (RES), digital input (Din), and latch enable ($\overline{\text{LE}}$) signals. c, Signals acquired by an oscilloscope showing the control sequence of the pulse-echo sensing and transducer multiplexing. d, Signals acquired by an oscilloscope showing the input sequence to the shift register for multiplexing and driving the transducer elements. All figure panels share the same color encoding scheme.

The AFE and the DAQ modules are interconnected by serpentine wires that allow for folding to minimize their footprint (Fig. 1.8). An elastomeric encapsulation mitigates strain concentrations and protects the circuit from irreversible deformations. The fully integrated system can be bent, stretched, and twisted (Fig. 1.9) and be conformally laminated on the human body (Fig. 1.10).

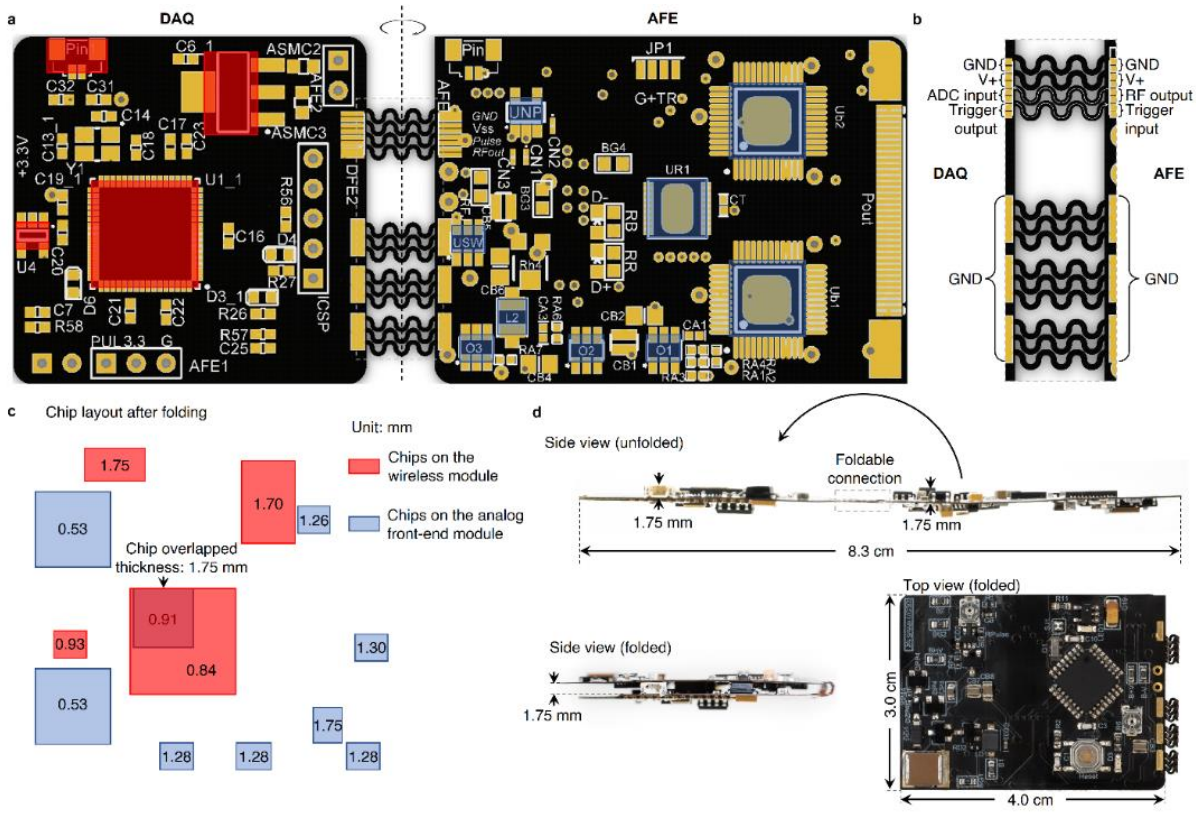

Figure 1.8: Foldability of the fPCB. a, The modular design of the circuitry consisting of the wireless data acquisition (DAQ) and the analog front-end (AFE) modules. The rigid chips with a thickness of more than 0.5 mm are highlighted with colored boxes. b, A zoomed-in view showing the serpentine interconnects between the DAQ and the AFE module. The power supply wires connect the battery voltage (V+) and the ground (GND) between two modules. The AFE outputs radiofrequency (RF) signals, which are received by the DAQ as the input to the analog-to-digital converter (ADC). Meanwhile, the DAQ module outputs trigger signals, which are received by the AFE as the input to initiate pulse-echo sensing. c, The chip layout was designed to reduce the thickness of the fPCB when folded. After folding, the board-to-board spacing is determined by two components (Pin as battery connectors, and inductor L2) with a thickness of 1.75 mm. Note that the overlapped chips (UR1 and U1_1) are of the same 1.75 mm thickness. Thus, the overlap does not add additional thickness to the folded device. d, Side views of the fPCB before and after folding. The folded DAQ and AFE modules have a minimum separation of 1.75 mm. The footprint of the entire fPCB is reduced from 3 cm by 8.3 cm to 3 cm by 4 cm after folding.

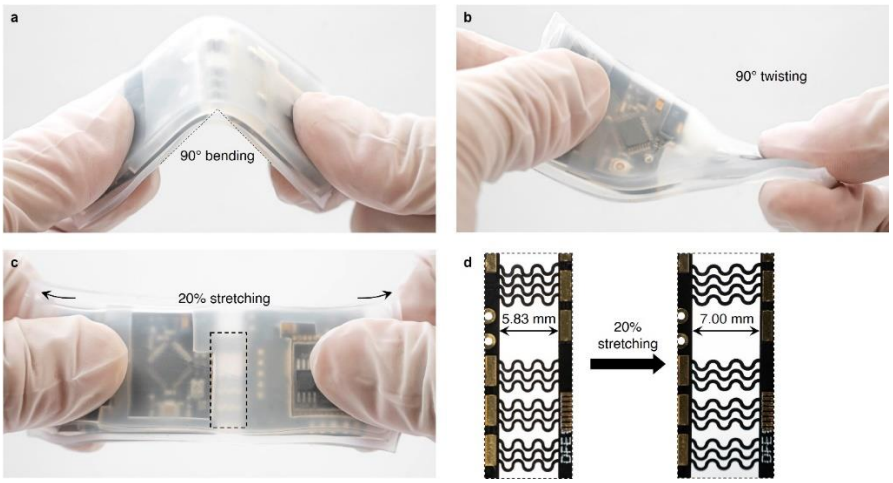

Figure 1.9: Deformation of the packaged USoP. a, 90° bending, b, 90° twisting, and c, 20% uniaxial stretching of the packaged USoP. d, A zoom-in view of the stretched interconnects.

Table 1.1: Key components used in the control electronics. All of the components are commercially off the shelf.

Component designator	**Description**	**Manufacture product number**
1,2	Multiplexer	MAX14866UTM+T
3	T/R switch	MD0101K6-G-ND
4	Operational amplifier	ADA4895-1ARJZ-R7
5,6	Operational amplifier	ADA4897-1ARJZ-RL
7	Single-pole double-throw analog switch	TS5A3159ADBVR
8	Voltage inverter	MAX829EUK
9	Zener diode	BZD27B18P-M3-08
10	Zener diode	BZX100A
11,12,13	Schottky diode	SB01-15C-TB-E
14,15	MOSFET-N	CPH3459-TL-W
16	Schmitt-trigger inverter	SN74LVC1G14DRLR
17	Microcontroller	ATMEGA328P-ANR
18	Voltage regulator	MIC5205-3.3YM5-TR
19	Voltage regulator	AMS1117
20	Microcontroller with ADC	PIC32MZ1024EFH064-I/MR
21	Voltage regulator	MIC5365-3.3YC5-TR
22	Wi-Fi module	ESP32-S3-WROOM-1

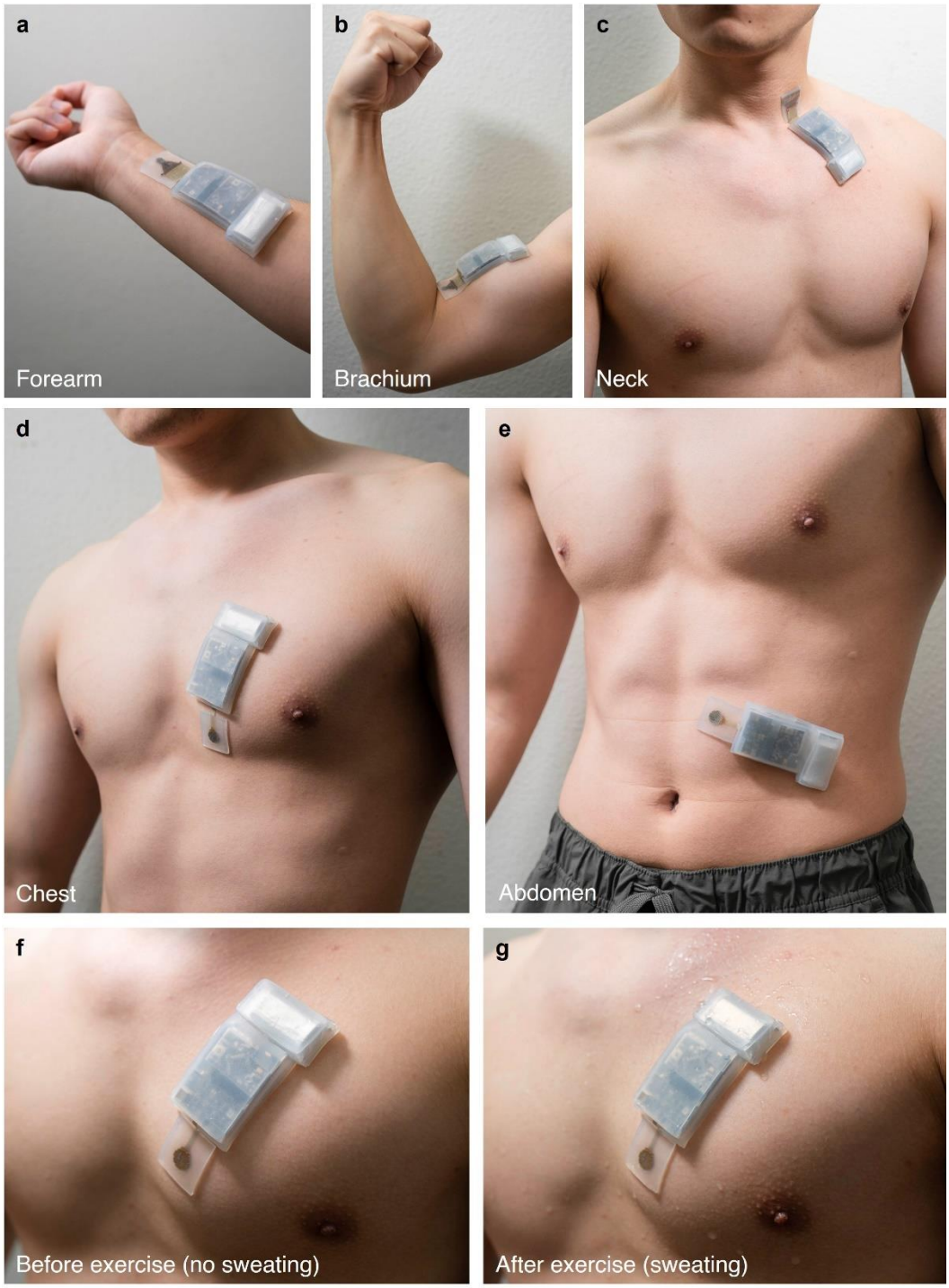

Figure 1.10: Skin integration of the conformal USoP device. The soft patch could conform to multiple curved body parts, including a, forearm, b, brachium, c, neck, d, lower chest, and e, abdomen. f-g, Skin integration of the device before and after exercise. The USoP could maintain robust adhesion to the skin after the subject performs intensive exercise and sweats.

Achieving high sensing bandwidths and sampling rates is critical for the circuitry design. In this work, the DAQ has a sampling rate of 12 Msps corresponding to a sensing bandwidth of 6 MHz. The Wi-Fi module can transmit such wide-band signals at a distance of ~10 m and a speed of 3.4 Mbps with zero data loss[26]. The USoP system has a power consumption of ~614 mW. A standard 3.7 V commercial lithium-polymer battery can enable continuous operation for up to 12 hours (Fig. 1.11).

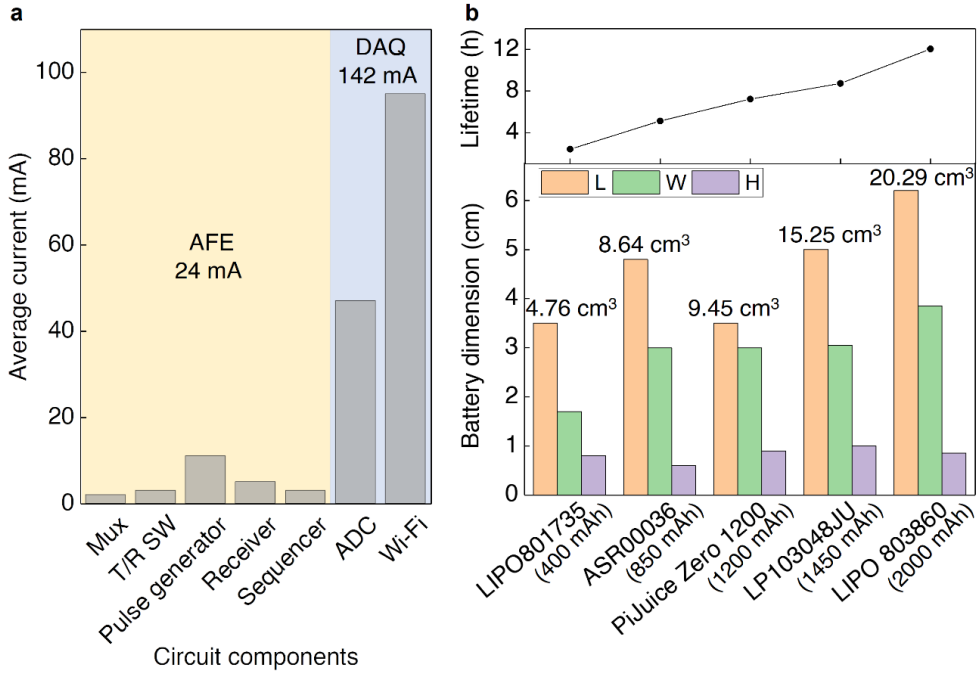

Figure 1.11: Power consumption and battery life of the USoP. a, Current consumption of the circuit components with a 3.7 V input. The total average current consumption is 166 mA (24 mA for the analog front end (AFE) and 142 mA for the wireless data acquisition (DAQ) module). Thus, the power of the USoP is ~614 mW. b, Lifetimes (upper panel) and the corresponding length (L) width (W), and height (H) (lower panel) of commercial batteries. By increasing the battery capacity and size from 400 mAh, 4.76 cm3 to 2 Ah, 20.29 cm3, the USoP can continuously operate for 2.4 h ~12.0 h.

The USoP is designed to support multiple ultrasound sensing modes, including amplitude mode (A-mode), motion mode (M-mode), and brightness mode (B-mode). A-mode is a fundamental sensing mode where the ultrasonic probe interrogates the tissue as a one-dimensional

depth recorder and produces a graph of the echo amplitude against the acoustic time-of-flight. An ultrasound beam was generated to penetrate the tissue layers, and then the beam was reflected by tissue interfaces of mismatched acoustic impedances. The tissue impedance information was then encoded in the amplitudes of the ultrasonic reflections, while the depth information was encoded in the acoustic time-of-flight. An example of A-mode sensing is shown by the arterial diameter measurement using a 4 MHz probe (Fig. 1.12a left). The posterior and anterior wall reflections were captured as the local maximums in the echo amplitude. Based on the echo amplitude signal, the arterial diameter could be calculated from the acoustic time-of-flight and acoustic speed in tissues (Fig. 1.12a right). M-mode can be considered as continuous A-mode sensing. In M-mode, the echo amplitude is instead encoded as the brightness of the pixel, freeing up one axis of the graph for temporal information. Therefore, M-mode can capture the motion of tissue interfaces over time along a one-dimensional scanning line, providing sensing resolution in depth (y-axis) and in temporal domains (x-axis). In M-mode, the ultrasonic beams were repetitively transmitted to tissues for continuous sampling. During each cycle of transmission, one frame of A-mode signal was generated. By converting the A-mode frames into grey-scale pixels columns and plotting these columns as a function of time, M-mode images could be generated. An exemplary application capturing the carotid artery pulsation suggests that M-mode images can continuously capture the arterial distensions using a 4 MHz linear array. Two frames of radiofrequency echo signal show the minimum and maximum arterial diameters (Fig. 1.12b left), which correspond to the diastolic and systolic phases of the arterial pulsation (Fig. 1.12b right).

Moreover, when a probe with 2D layout is used in M-mode sensing, not only the axial resolution but also the spatial distribution of the motion can be acquired. Each transducer in the

2D array can generate an independent beam for M-mode sensing, and the amplitude of tissue movements was then calculated to locate the position of maximum motion amplitude. Such a sensing mode can be used for spatial detection of target arteries or guiding catheterization. As a demonstration, I mapped the arterial pulse waveform at the brachium using a 6 MHz 2D layout probe. The arterial pulse amplitudes and the mapped location of the brachial artery are shown in Fig. 1.12c.

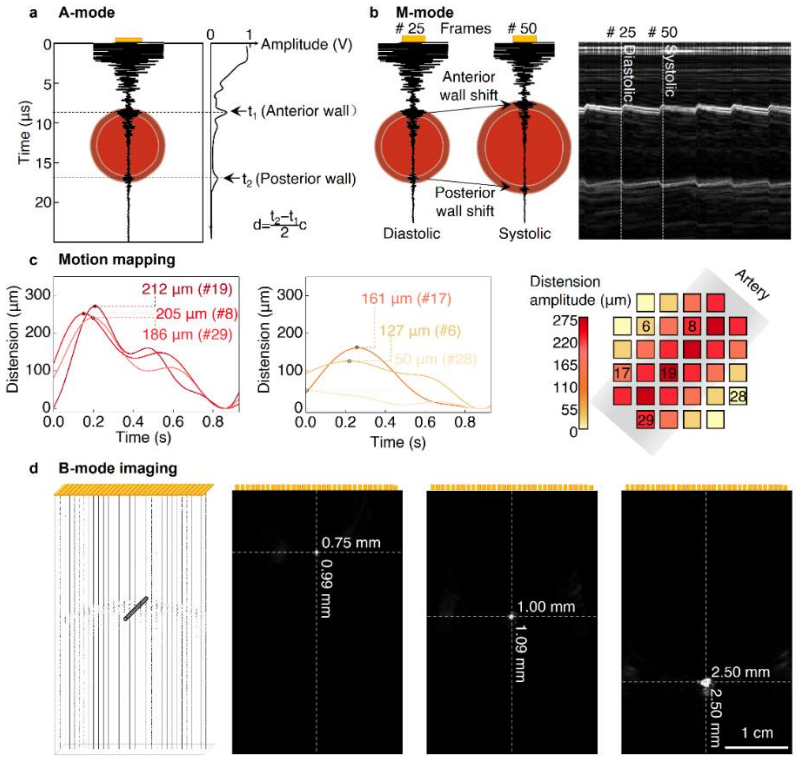

Figure 1.12: Multi-mode sensing with wearable ultrasonic probes. a, Amplitude mode (A-mode) for capturing arterial walls. Envelopes of radiofrequency signals indicate the amplitudes and positions of the reflection interfaces. The arterial diameter (d) is then the product of one half of the acoustic time-of-flight (t2-t1) and acoustic speed (c). b, Motion mode (M-mode) for capturing the distensions of arterial walls continuously. Exemplary frames of radiofrequency signals (left) with corresponding diastolic and systolic phases in the M-mode image (right). c, Motion mapping of the brachial artery using the 6 MHz 2D probe. Based on the distension amplitudes (left and middle), the spatial orientation of the brachial artery can be mapped (right). d, Brightness mode (B-mode) imaging of an iron wire phantom using a 2 MHz linear array probe. Radiofrequency signals (left) illustrate the reflected wavefront of the iron wire. Reconstructed images (right) show the imaged iron wire at depths of 1 cm, 2 cm, and 3 cm. The axial and lateral full widths at half maximum are labeled on the images showing the imaging resolution of the linear array at different depths.

In addition, the soft probes that conform to highly curved skin surfaces may experience phase distortion. Therefore, The the image stability with array distortions is characterized in both elevational and azimuth planes. The elevational distortion is not critical for either A-mode, M-mode applications, or B-mode imaging when the probe's elevational aperture is small, because the smaller the elevational aperture, the smaller the time delay error caused by array bending (Fig. 1.13a,b). I simulated the transmission beam patterns at varying bending curvatures (from 6 mm to ∞) (Fig. 1.13c). Although the beam patterns suggest bending may introduce undesired side lobes, the intensity of these lobes is much smaller than the main lobe (Fig. 1.13d). Additionally, when the bending curvature radius is >6 mm, the transmission beam pattern would have negligible widening (Fig. 1.13e). Considering typical body parts have surface curvature radii much larger than 6 mm, the elevational distortion induced by human studies could be neglected.

While the elevational distortion would not affect imaging applications, the azimuth distortion may compromise the B-mode imaging if the array deformation exceeds a safety threshold. Because beamforming requires accurate positioning of each transducer in the array to calculate the delay function, a bent array would cause phase aberration and resolution degradation. I simulated the B-mode images of point sources to quantify the effect of bending curvature on the images (Fig. 1.14). With the bending curvature radii <6 cm, the B-mode images show artifacts in the shallow area (Fig. 1.14b, upper panels). When the bending curvature radii ≥6 cm, the imaging quality is acceptable without obvious artifacts (Fig. 1.14b, lower panels). Considering most body surfaces have curvature radii larger than 6 cm, the imaging results could be reliable.

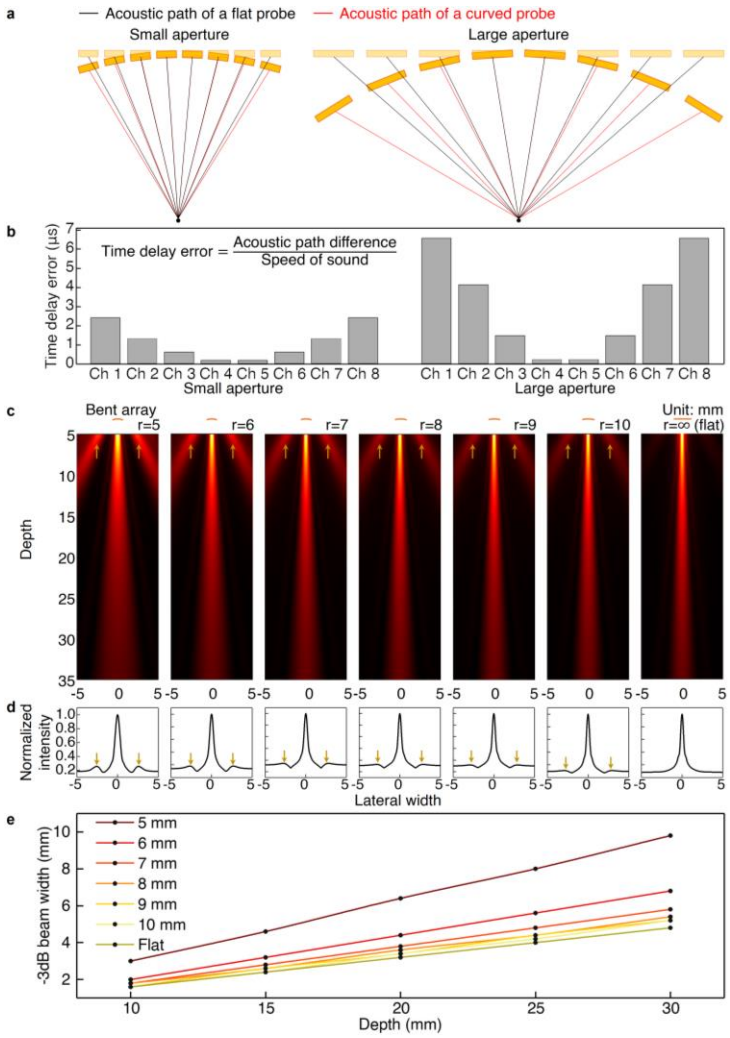

Figure 1.13: The transmission beam patterns with elevational deformation. a, Schematics showing two arrays bent at a curvature of 10 mm-1. Both devices have 8 transducers. The small aperture device has a pitch of 0.8 mm, while the large aperture device has a pitch of 1.6 mm. A point source is set at 5 cm away from the array center. b, Corresponding time delay errors were calculated for each transducer. c, Simulated elevational beam patterns of the 4 MHz linear array. The probe was bent elevationally with radii of 5~10 mm and the beam patterns were compared with a flat array. d, Beam intensity profiles at a depth of 5 mm showing the side lobe intensities are <30% of the main lobe at all bending curvatures. e, -3dB beam width suggesting the bending is not generating significant beam widening when the bending radius is >6 mm.

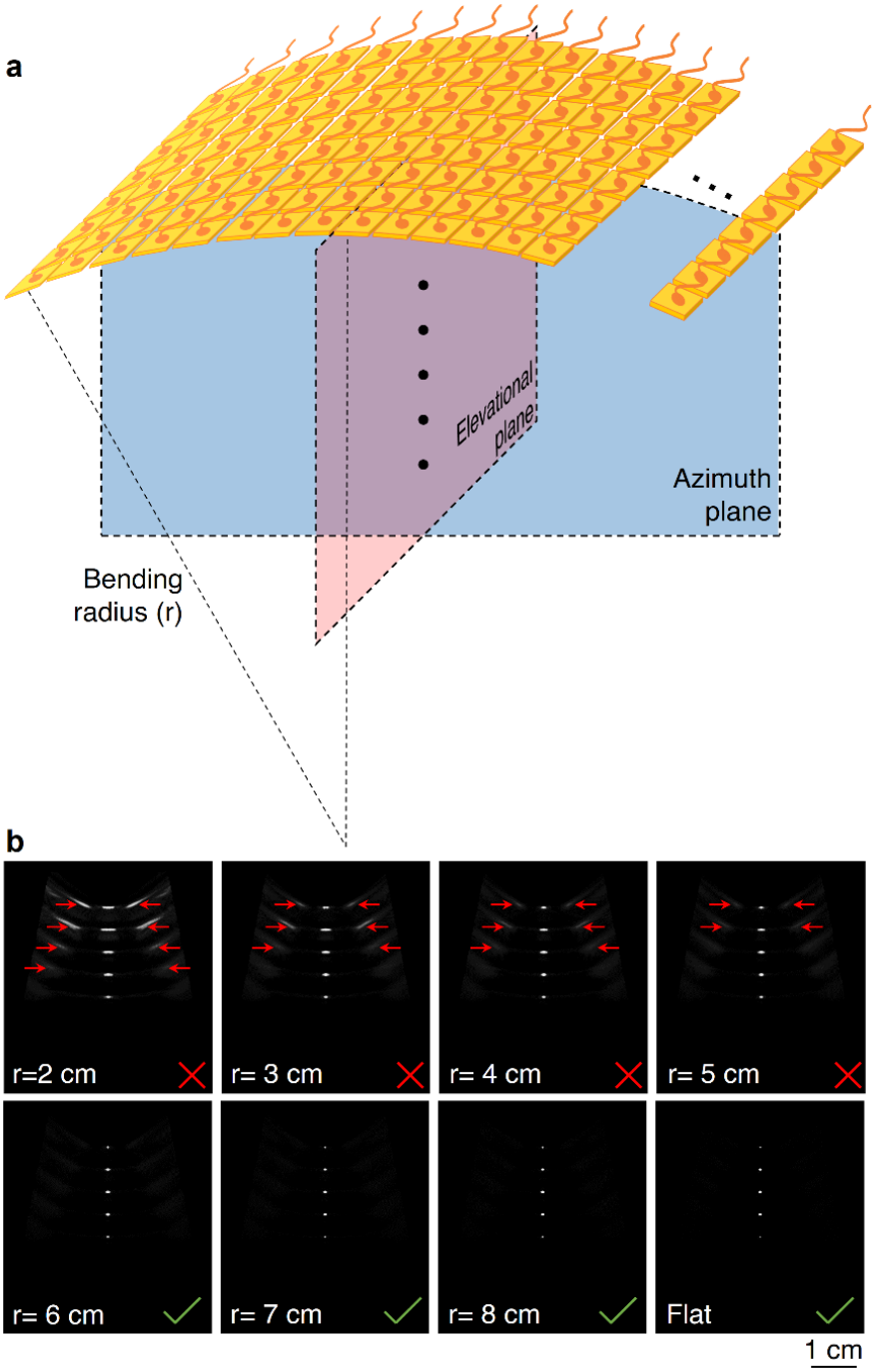

Figure 1.14: Simulated B-mode images of point sources with azimuthal bending. a, Schematics showing a bent linear array along the azimuthal direction. b, B-mode imaging results of point sources at depths of 1 cm, 1.5 cm, 2 cm, 2.5 cm, and 3 cm by a 4 MHz linear array with different bent radii. The results suggest artifacts (labeled with red arrows) would appear when the array is bent with a radius <6 cm.

Acknowledgements

Chapter 1, in full, is a reprint of the material as it appears in Nature Biotechnology. Muyang Lin, Ziyang Zhang, Xiaoxiang Gao, Yizhou Bian, Ray S. Wu, Geonho Park, Zhiyuan Lou, Zhuorui Zhang, Xiangchen Xu, Xiangjun Chen, Andrea Kang, Xinyi Yang, Wentong Yue, Lu Yin, Chonghe Wang, Baiyan Qi, Sai Zhou, Hongjie Hu, Hao Huang, Mohan Li, Yue Gu, Jing Mu, Albert Yang, Amer Yaghi, Yimu Chen, Yusheng Lei, Chengchangfeng Lu, Ruotao Wang, Joseph Wang, Shu Xiang, Erik B. Kistler, Nuno Vasconcelos & Sheng Xu. "A fully integrated wearable ultrasound system to monitor deep tissues in moving subjects." Nature Biotechnology, 2023. The dissertation author was the primary investigator and author of this paper.

Chapter 2 Physiological signal recording and validation

In clinical practice, A-mode and B-mode are commonly used for temporary measurements, while M-mode is for monitoring signals continuously[27]. Additionally, M-mode is valuable for quantitatively characterizing tissue dynamics[28-30]. Therefore, in this work, focusd imaging modality of the USoP in M-mode. Natural physiological processes, such as circulation and respiration, can be manifested in the motion of tissue interfaces, such as myocardial contraction, arterial pulsation, and diaphragmic excursion. The USoP can quantify these interfacial motions from multiple sensing windows in the human body (Table 2.1 and Fig. 2.1a).

Table 2.1: The typical depths and motion magnitudes of different tissue interfaces. The interfaces in this study include the arterial walls, ventricular wall, and diaphragm dome.

Tissue interface	**Depth**	**Motion scale**
Radial artery wall	1.00-4.00 mm	0.01-0.06 mm
Brachial artery wall	3.0-8.1 mm	0.04-0.17 mm
Common carotid artery wall	4.4-30.4 mm	0.26-0.90 mm
Common femoral artery wall	10-140 mm	0.15 mm-1.00 mm
Abdominal aorta wall	40-100 mm	0.57 -2.00 mm
Ventricular wall	69.9-92.7 mm	12.2-16.2 mm
Diaphragm	100-181.7 mm	8.0-42.0 mm (normal breath) 52.7-92.1 mm (forced breath)

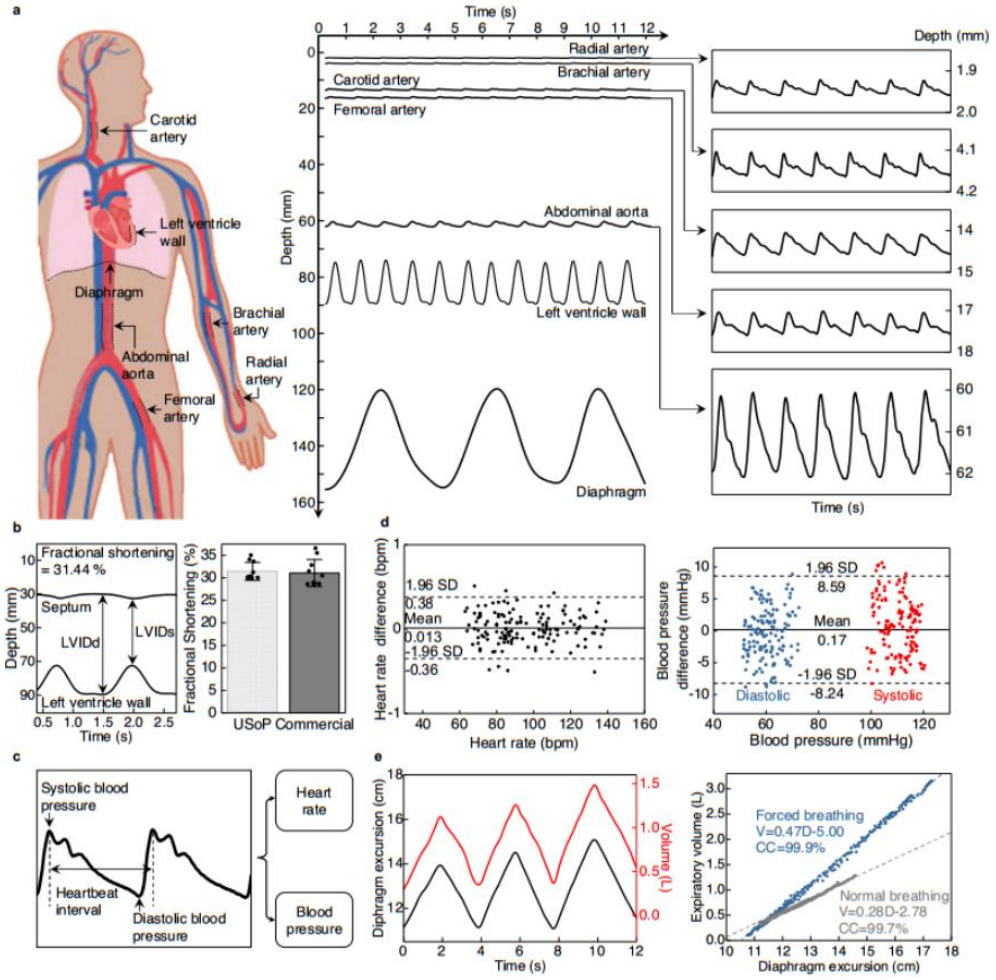

Figure 2.1: Monitoring and analysis of tissue interface motions using the USoP. a, Schematics and measurement results of seven representative dynamic tissue interfaces. b, Deriving physiological parameters from myocardial contraction. From the M-mode waveforms of the septum and left ventricular wall, the left ventricular internal diameter at end-diastole (LVIDd) and end-systole (LVIDs) can be used to derive the fractional shortening (left). Comparison of measurements between the USoP and a commercial ultrasound probe (right). The results are averaged from ten independent measurements, and the error bars represent the standard deviation (SD). c, Derivation of physiological parameters from the arterial pulse waveforms, including the heart rate and blood pressure. d, Bland-Altman plot showing measurement agreement between the USoP and a tonometer. For the heart rate, a mean difference of 0.013 beats per minute is observed, and 135 of 142 (95.1%) data points are within 95% limits of agreement defined by $\pm$ 1.96 SD (left). For the blood pressure, a mean difference of 0.17 mmHg is observed, and 269 of 280 (96.1%) data points are within 95% limits of agreement defined by ±1.96 SD (right). e, Derivation of expiratory volume from the diaphragmatic excursion. Simultaneous measurements of diaphragmatic excursion and respiratory volume show a similar pattern (left). The regression on expiratory volume (V) with diaphragmatic depth (D) in normal breathing and forced breathing. Strong linear relationships, with correlation coefficients (CCs) close to 100%, can be found between the diaphragmatic excursion and expiratory volume in both breathing conditions (right).

The motion of tissue interfaces can be continuously captured using M-mode sensing. By transmitting ultrasound beams into tissues at a pulse-repetitive-frequency of 25 Hz~1 kHz, the displacement of various dynamic tissue interfaces can be interrogated. Displacement of the tissue interfaces is encoded in radiofrequency echo signals. To decode the tissue motions, an auto-correlation method was deployed. In consecutively collected radiofrequency data frames, the echo from a tissue interface constantly moves within a specific range, shifting along the time axis but roughly maintaining its profile (Fig. 2.2a). To decode the motion amplitude, the ultrasound radiofrequency data were first segmented to exclude the signal without motion. Envelopes of the segmented signals were then generated. After that, the auto-correlation method was applied to the generated envelope to obtain the auto-correlation value between adjacent frames (Fig. 2.2b). The lag (t) between two adjacent frames could then be determined by the position of the maximum auto-correlation value (Fig. 2.2c). The motion, also known as the displacement between two frames, was calculated as half of the acoustic round trip $d=c\times t/2$. Noted that the auto-correlation decoding is based on envelope shifting, thus it is not sensitive to the transducer bandwidth or ringing in the radiofrequency signals as long as the envelope can roughly maintain its profile during shifting.

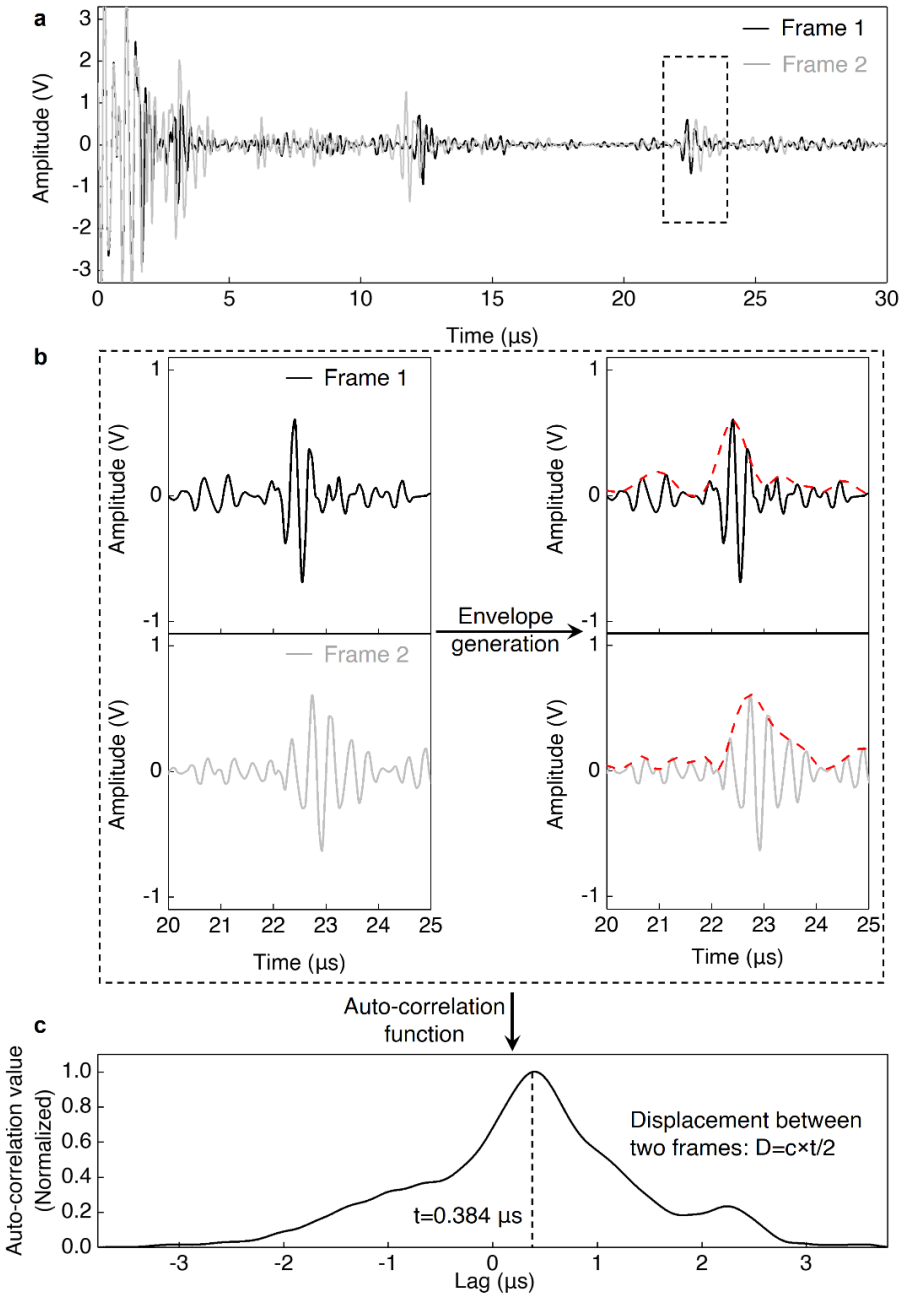

Figure 2.2: Tissue interfacial motion detection using the auto-correlation method. a, Two frames of radiofrequency echoes showing the motion of tissue interfaces. b, Segmented radiofrequency echoes containing the reflection from a tissue interface. The envelopes are generated from the echo segments to define the profile of the interfacial reflection. c, Auto-correlation value calculated from the envelopes. A lag of 0.384 μs corresponding to the maximum auto-correlation value is determined as the time delay between the two frames.

From myocardial contraction, the diameter change of the left ventricle during cardiac cycles can be recorded, and therefore fractional shortening can be derived as a measure of left ventricular function (Fig. 2b left)[31]. A comparison of measurements from the USoP and a commercial ultrasonic system shows a mean difference of ~1% (Fig. 2.1b right).

In arterial pulse waveforms, the pulse interval reflects the heart rate, and the pulse intensity can be correlated to blood pressure (Fig. 2.1c)[19]. From biomechanics, the measured pulse intensity effectively represents the arterial diameter change[19], which is a function of two variables: blood pressure and arterial stiffness. The blood pressure tends to expand the cross-section of the artery, while the arterial wall stiffness resists this expansion. The exponential relationship between the diameter and arterial stiffness is independent of the blood pressure at the time of measurement within the physiological range (63-200 mmHg)[32,33]. The equation can be used to derive[19,32]:

$$p(t)=p_d * e^{\beta\left(\frac{D(t)}{D_d}-1\right)}$$

and

$$\beta=\frac{D_d \ln\left(p_s/p_d\right)}{D_s-D_d}$$

where $p(t)$ is the time-dependent blood pressure and $D(t)$ is the time-dependent arterial diameter; D_s and D_d are the systolic and diastolic arterial diameters, respectively, derived from the measured pulse intensity; p_s and p_d are the reference systolic and diastolic pressures, respectively, measured using a commercial blood pressure cuff; and β is the stiffness index[32].

First, D_s, D_d, p_s, and p_d at the brachial artery of the subject were measured to obtain β, with the subject sitting upright in a chair with the measured arm relaxed on a table. Specifically,

p_s and p_d were measured using a commercial cuff as calibration. The arterial diameter was then measured at the same location using the USoP to derive D_s and D_d. Then, $p(t)$ was determined based on the corresponding $D(t)$ measured by the USoP. Measurement of $p(t)$ using the USoP is highly stable with little need for recalibration. The initial calibration using the commercial cuff only needs to be performed once at the beginning of this process, as p_d remains relatively stable from beat to beat[19]. The measurement of blood pressure using the USoP at the brachial artery is applicable to other arterial sites as well because β and p_d do not change significantly along the major branches of the arterial tree[19,34]. This allows us to equate brachial blood pressure measurements to the carotid blood pressure in healthy adults[35]. Note that β and p_d may change substantially on younger subjects[34] and patients with vascular diseases, such as carotid atherosclerosis[36]. In these populations, it may require accurate local carotid stiffness index and carotid blood pressure using catheterization to minimize the calibration error[37-39]. In addition, the body habitus of the subject may also influence the calibration accuracy. For example, the height of subject may influence vascular resistance and further influence blood pressure calibration[40]. In such cases, the vascular resistance could be estimated using nomograms or demographic databases[41], and then the stiffness index for blood pressure calibration could be corrected for better accuracy.

The USoP results are validated against a clinical-grade tonometer, the non-invasive gold standard for pulse waveform recording[42]. Bland-Altman analysis was performed to compare the waveform-derived heart rate and blood pressure from both devices (Fig. 2.1d). The 95% limits of agreement included >95% of differences between the results from the tonometer and USoP,

showing measurement consistency between these two devices. Additionally, the time difference between myocardial contraction and arterial pulsations can be used to quantify the pulse wave velocity, which correlates to the arterial stiffness of specific arterial segments (Fig. 2.3). Comparing the results of the USoP with those of the tonometer suggests a mean pulse transit time difference of <0.5 ms, which results in <4% error in pulse wave velocity recording, further demonstrating the accuracy of the USoP (Fig. 2.3)[43].

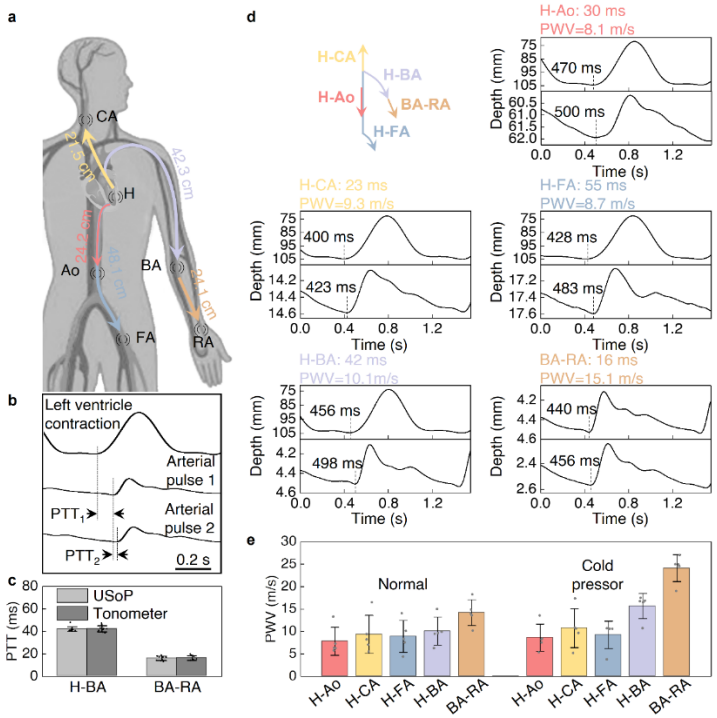

Figure 2.3: Pulse wave velocity (PWV) measurements. a, Schematic illustration of the pulse wave propagation paths in this study. Five paths were investigated, including the heart to the abdominal aorta (H-Ao), the heart to the carotid artery (H-CA), the heart to the femoral artery (H-FA), the heart to the brachial artery (H-BA), and the brachial artery to the radial artery (BA-RA). b, Pulse waveforms collected by synchronized USoP pairs. The pulse transit time (PTT) was defined as the delay between the diastolic feet of the ventricular contraction and arterial pulses. c, The averaged PTT values by the USoP and the tonometer, showing consistency for both H-BA and BA-RA. Ten consecutive pulses were recorded to calculate average PTT values. The error bars represent the measurement standard deviations. d, PWV calculated across five arterial segments using the USoP. e, PWV mapping under normal conditions and cold pressor test. The averaged PWV along each path was calculated from five independent measurements. The error bars indicate the standard deviations of the measured values. The PWV increases from heart-proximal to heart-distal branches. There is a regional increase of PWV in H-BA and BA-RA segments owing to cold-induced vasoconstriction.

The USoP can also measure diaphragmatic excursion as a surrogate for changes in respiratory volume due to breathing. The diaphragm depth recorded by the USoP is compared with the respiratory volume recorded by a spirometer (Fig. 2.1e left). With a linear regression model, the correlation coefficients between the diaphragmatic depth and respiratory volume under normal and forced breathing conditions are 99.9% and 99.7%, respectively (Fig. 2.1e right). Furthermore, these derived volumes can be used to characterize respiratory performance and identify airway obstruction or lung capacity restriction (Fig. 2.4, and Table 2.1), which can potentially be used for screening respiratory issues such as chronic obstructive pulmonary disease[44] and pulmonary fibrosis[45].

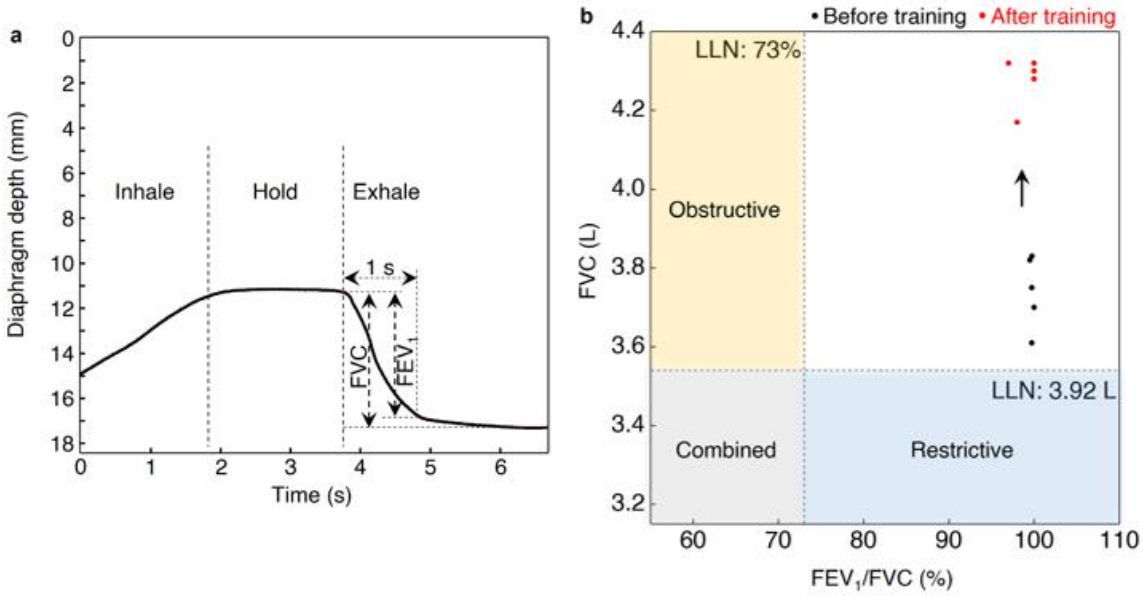

Figure 2.4: Calculations of expiratory volumes. a, Diaphragm motion during forced expiration recorded by the USoP. In the exhaling phase, the total excursion (FVC) and the excursion within the first second of exhaling (FEV1) were recorded. b, Based on the measured FEV1 and FVC, the respiratory function of a healthy volunteer was evaluated. The volunteer performed the same FEV1 and FVC measurements after participating in aerobic training ~5 hours per week for four consecutive months. The four-quadrant plot suggests an increased FVC, indicating an enhanced expiratory function. Unhealthy respiratory performance, such as obstructive, restrictive, and combined conditions, could be diagnosed if the FVC and FEV1/FVC values are below the lower limit of normal (LLN).

Table 2.1: Summary of typical expiratory volumes and their measurements. Clinical measurements of FVC, FEV1, and the derived parameter FEV1/FVC are used for diagnosing different respiratory issues.

Full name	**Clinical measurements**
Forced vital capacity (FVC)	Total volume achieved by the quickest possible exhalation after a maximal inhalation
Forced expiratory volume in one second (FEV_1)	Volume achieved in the first second by the quickest possible exhalation after a maximal inhalation
FEV_1/FVC	Forced expiratory volume measured in the first second as a percentage of forced vital capacity

Acknowledgements

Chapter 2, in full, is a reprint of the material as it appears in Nature Biotechnology. Muyang Lin, Ziyang Zhang, Xiaoxiang Gao, Yizhou Bian, Ray S. Wu, Geonho Park, Zhiyuan Lou, Zhuorui Zhang, Xiangchen Xu, Xiangjun Chen, Andrea Kang, Xinyi Yang, Wentong Yue, Lu Yin, Chonghe Wang, Baiyan Qi, Sai Zhou, Hongjie Hu, Hao Huang, Mohan Li, Yue Gu, Jing Mu, Albert Yang, Amer Yaghi, Yimu Chen, Yusheng Lei, Chengchangfeng Lu, Ruotao Wang, Joseph Wang, Shu Xiang, Erik B. Kistler, Nuno Vasconcelos & Sheng Xu. "A fully integrated wearable ultrasound system to monitor deep tissues in moving subjects." Nature Biotechnology, 2023. The dissertation author was the primary investigator and author of this paper.

Chapter 3 Machine learning-assisted autonomous data analysis

The USoP with a 4 MHz 32-channel linear array probe is used to autonomously and continuously track the position of the carotid artery and sense its pulsations. The linear array has an acoustic aperture of ~25.4 mm, which is sufficiently wide to accommodate the misalignment between the probe and the carotid artery[46]. Pulsation is visible in the M-mode images derived from the transducer channels directly above the carotid artery, while the M-mode images from the other adjacent channels show weaker or no pulsations (Fig. 3.1a). I train machine learning models to classify those M-mode images and identify whether salient pulsation patterns are present in the image (Fig. 3.2). Specifically, I use a VGG13 model because it outperforms other commonly used models for medical image classification in terms of precision, recall, and accuracy. This model can even robustly handle compromised ultrasound images and maintain the precision, recall, and accuracy higher than 98.4% (Fig. 3.3). Based on the arterial wall patterns in the M-mode images, this model predicts probability scores for each of the 32 channels and, therefore, generates a probability profile of the position of the artery. The probability profile is generated through convolving the raw prediction profile with a one-dimensional Gaussian kernel function. In my experiments, this was sufficient to produce a bell-shaped curve that reliably determines the position of the arterial center. The channel with the highest probability is determined as the center of the artery, and its channel data is used for generating the pulse waveforms (Fig. 3.1b).

Figure 3.1: Autonomous and continuous blood pressure recording in a moving subject. a, Schematic cross-sectional view of a soft 4 MHz linear array sensing the carotid artery (left). Representative M-mode images of channels with beam penetrating or not-penetrating the carotid artery, classified as carotid artery (CA) or non-carotid artery (nCA) images, respectively (right). b, Flow diagram showing the process of autonomous CA detection and pulse waveform generation. c, Recording in a moving subject using the USoP with and without an autonomous algorithm. The algorithm can reliably track the CA position with head yawing from -80° to +80°, corresponding to a ~19 mm CA displacement. Prediction scores of different transducer channels for tracking the CA at each yawing position and corresponding B-mode images collected by a commercial ultrasound machine (upper panel). By actively selecting the best channel to follow the CA motion (e.g., #5, #8, #16, #23, and #29), continuous pulse waveforms can be recorded. In contrast, without the auto-selection algorithm, a fixed channel (#16) results in signal loss during motion (lower panel). d, Two representative M-mode images recorded from the training subject (#1) and a new subject (#2), showing different image patterns (left). The histograms of the two CA images show a substantial difference in luminosity distribution (right). Inset: subject #2 has ~six times more white pixels than subject #1, indicating thicker arterial walls. e, Schematic diagram showing the workflow of the minimal entropy correlation alignment model, consisting of two encoders with five convolutional (Conv.) layers and three fully connected (FC) layers. The classification loss and geodesic covariance loss are used to align features extracted from the training image set (source domain) and those from a new image set (target domain). f, Model generalizability validation on 10 subjects. The classification model is trained on each subject and validated on the remaining subjects. Without domain adaptation, the matrix plot shows an average classification accuracy of only 63.23% on new subjects (left). After domain adaptation, the average classification accuracy is boosted to 96.13%, showing the improved generalization of the classification model (right).

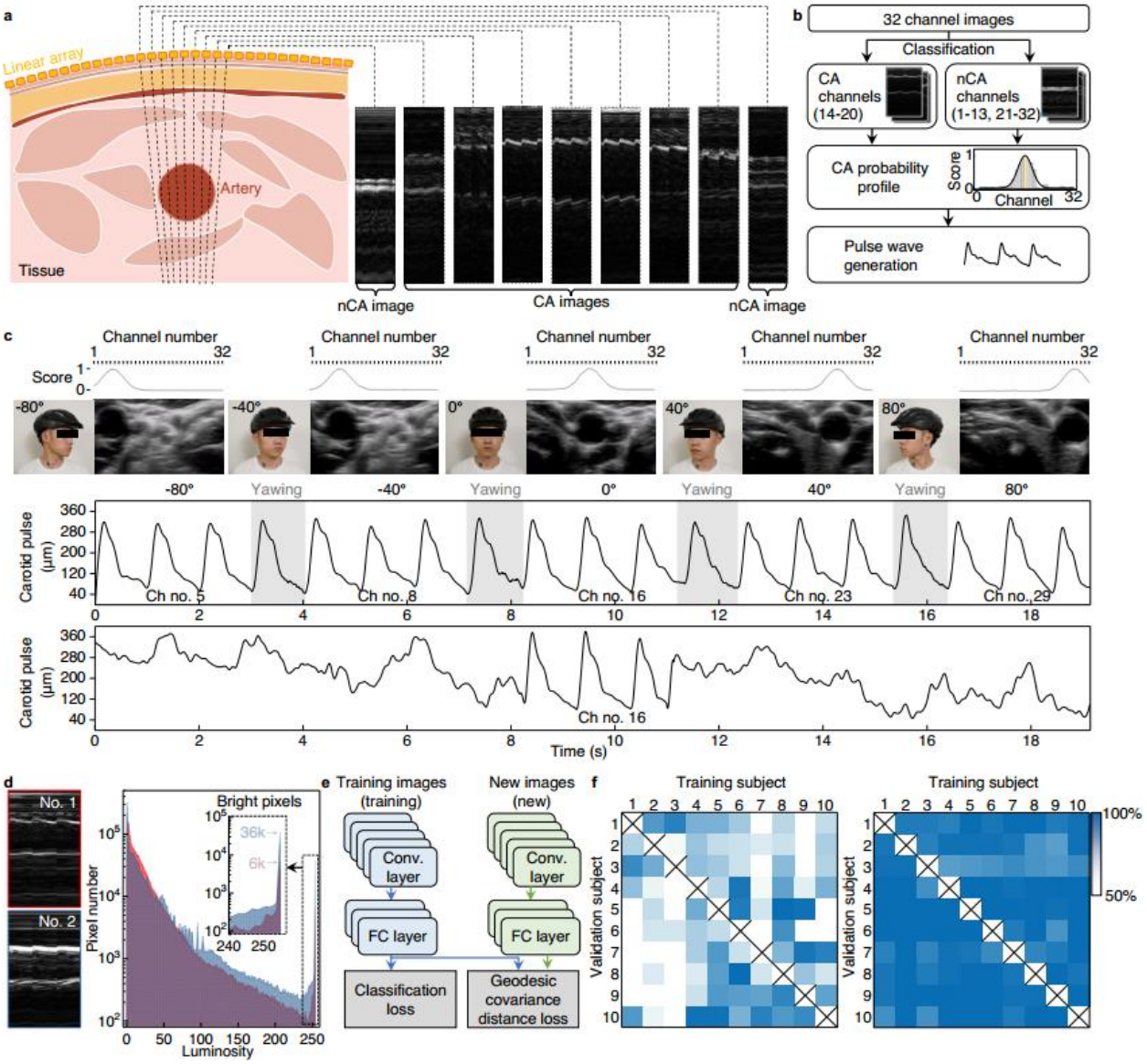
a
Linear array
Artery
Tissue
nCA image
CA images
nCA image
b
32 channel images
Classification
CA channels (14-20)
nCA channels (1-13, 21-32)
CA probability profile
Score
Channel
Pulse wave generation
c
Channel number
Score
-80°
-40°
0°
40°
80°
Yawing
Carotid pulse (μm)
Ch no. 5
Ch no. 8
Ch no. 16
Ch no. 23
Ch no. 29
Time (s)
d
No. 1
No. 2
Bright pixels
36k
6k
Pixel number
Luminosity
e
Training images (training)
New images (new)
Conv. layer
FC layer
Classification loss
Geodesic covariance distance loss
f
Training subject
Validation subject
100%
50%

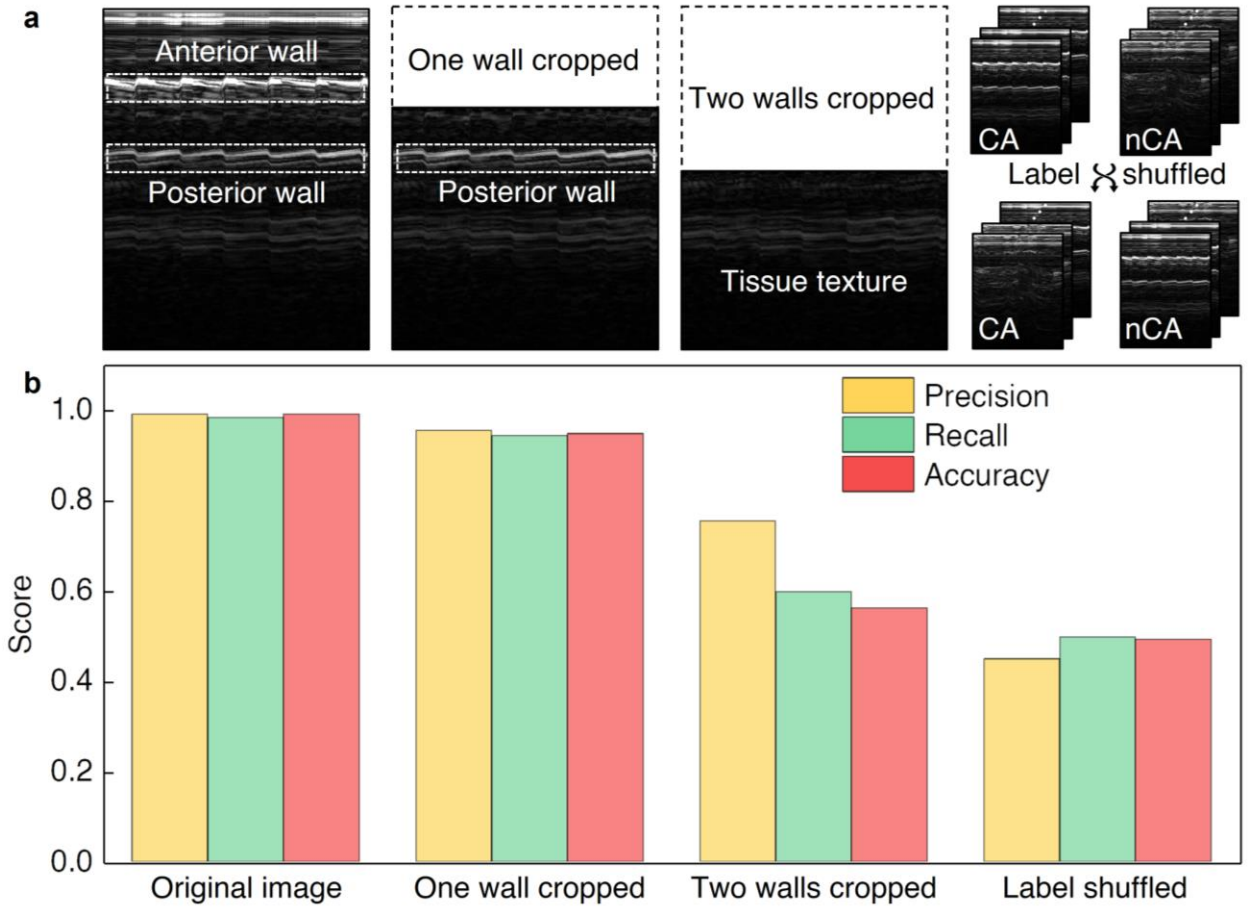

Figure 3.2: Model training and validation with modified datasets. a, Modifications to the original image datasets, including one wall cropped, two walls cropped, and label-shuffled images. b, The VGG13 model validation metrics on these modified datasets. The training/validation was conducted on a modified dataset of 3826 ultrasound images with a 1:1 training/validation split.

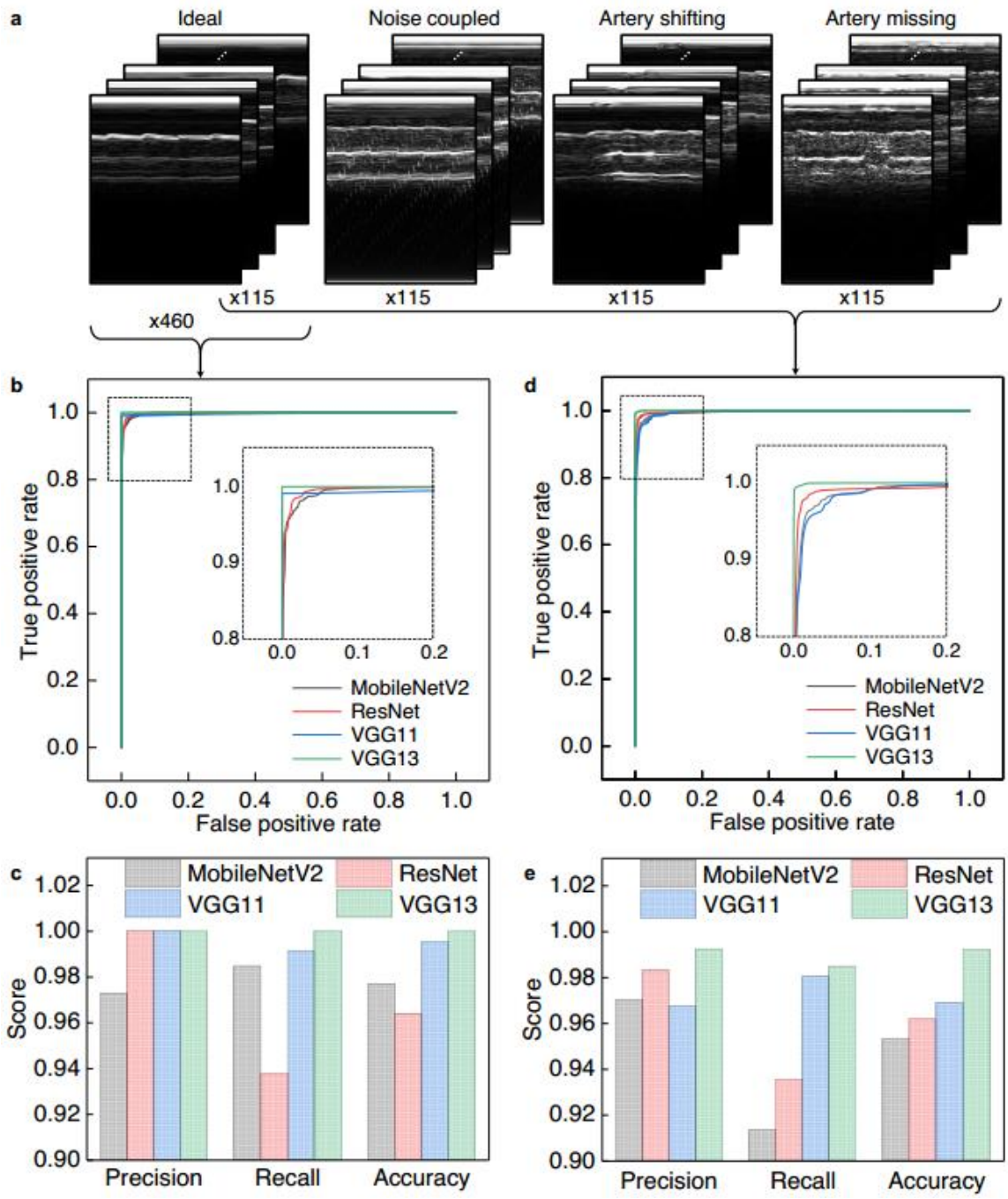

Figure 3.3: The validation metrics of four models on ideal and compromised image datasets. a, The images used for validation including ideal carotid artery images and compromised images (e.g., noise coupled images, artery shifting images, artery missing images). b, The receiver operating characteristic curves validated on 460 ideal images, suggesting the best model VGG13 has an area under the curve value of 100%. c, The precision, recall, and accuracy validated on ideal images. d, The receiver operating characteristic curves validated on 460 images with a mix of ideal and compromised images, suggesting the best model VGG13 has an area under the curve value of 99.4%. e, the precision, recall, and accuracy validated on mixed ideal and compromised images.

The human head motion is recorded using inertia measurement units (Fig. 3.4) and simultaneously image the carotid artery to quantify its displacement. The head can yaw at a larger angle than it can roll and pitch, and yawing generates the largest arterial displacement (>10 mm). The USoP generates M-mode images from all channels with head yawing. The VGG13 model identifies the M-mode images containing arterial pulsations, determines a moving sub-aperture to follow the carotid artery, selects the optimal channel from the probability profile, and generates continuous pulse waveforms autonomously (Fig. 3.1c). In contrast, without the model, a fixed channel with head yawing generates inaccurate pulsation measurements or loses track of the pulsation waveform once the artery is outside its sensing aperture (Fig. 3.1c). The model prediction remains reliable at a head yawing rate <60°/s. At yawing rates beyond this limit, the pulse waveform becomes distorted but is quickly restored when motion stops (Fig. 3.5).

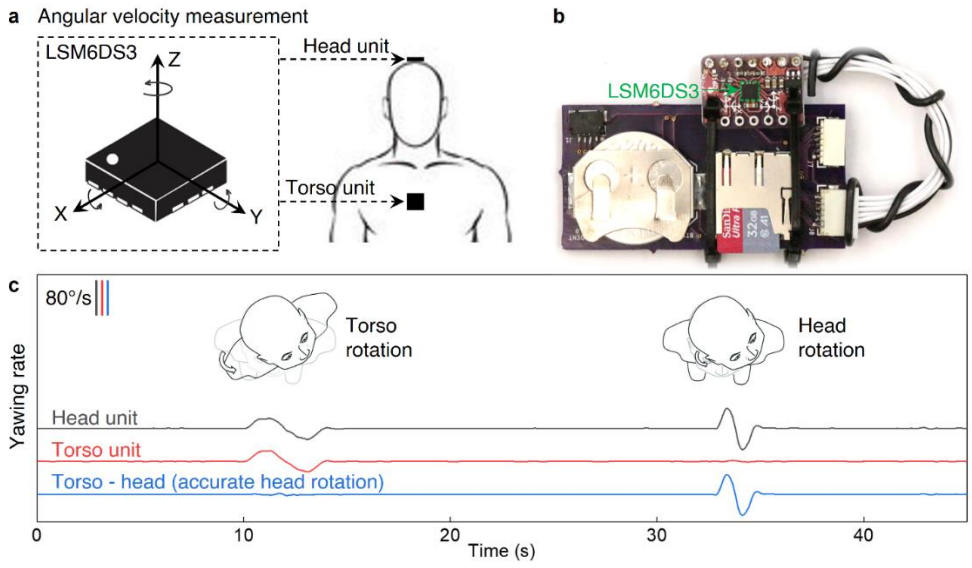

Figure 3.4: Recording head rotation. a, Two separate inertial measurement units (LSM6DS3) were mounted on the head and chest of the participant to record head rotation. b, The circuit to interface LSM6DS3, which had a memory card to save the recordings for post-processing. c, The recorded yawing rates while the participant was performing torso rotation and head rotation. By calculating the difference between the head unit and the torso unit, the torso motion could be removed and thus, accurate head rotation could be recorded.

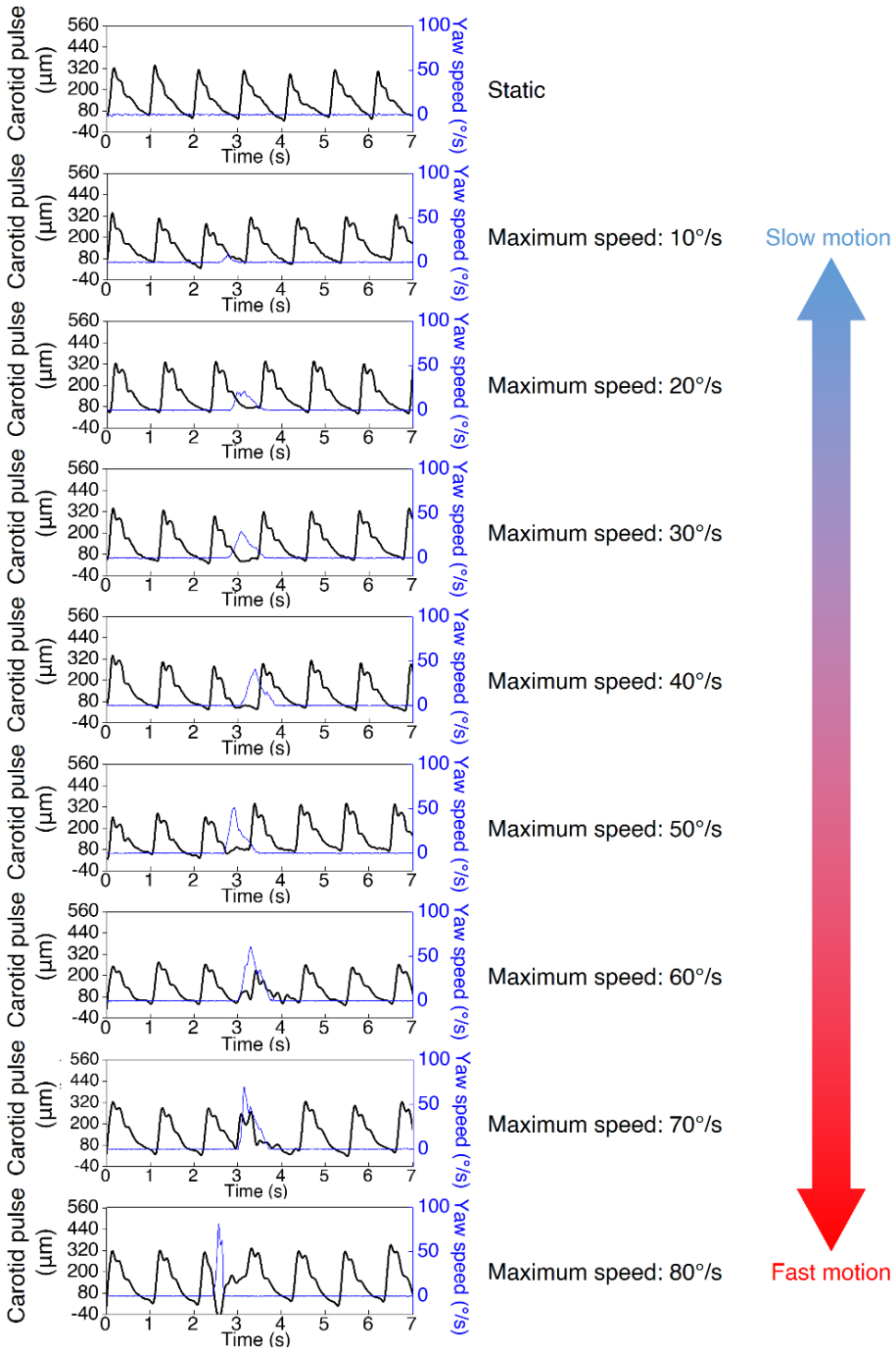

Figure 3.5: Recorded pulse waveforms under increasing yawing rates from 0°/s to 80°/s. Under slow motions, the carotid pulse waveforms show high continuity. When the yawing rate increases to 70°/s and 80°/s, the waveforms start to show obvious distortions.

Machine learning algorithms may encounter generalization problems when tested on images outside the training pool. For example, images from a new subject may have distinct

brightness, contrast, and arterial wall patterns, which would result in different luminosity distributions (Fig. 3.1d). The generalization of the VGG13 model is enhanced by using domain adaptation with a minimal entropy correlation alignment model[47] (Fig. 3.1e) to transfer the machine learning network to new image datasets without additional labeling. The use of domain adaptation allows the model to generalize to different subjects. A t-distributed stochastic neighbor embedding visualization of the subject distributions shows that images from different subjects are unified after domain adaptation is applied. Model generalizability is demonstrated through cross-validation among 10 subjects (Table 3.1). The classification model is trained on each subject and then validate it on the nine other subjects. Without domain adaptation, the model only has an average accuracy of 63.23% on new subjects (Fig. 3f left). After domain adaptation, this accuracy increases to 96.13% (Fig. 3f right). The minimum data required to be collected from a new subject for successful domain adaptation is also investigated. The results showed that only 32 unlabeled images from a new subject suffice to achieve >90% classification accuracy (Fig. 3.6).

Table 3.1: Demographic characteristics of the participants in this study. They vary in gender, race, age, height, weight, and body-mass index, which generate diversity in the collected ultrasonic images.

Gender	**n (percentage)**
Male	6 (60%)
Female	4 (40%)
Race	**n (percentage)**
Asian	5 (50%)
Hispanic or Latino	3 (30%)
White	2 (20%)
At time of study	**Mean ± Standard deviation**
Age (years)	27.78 ± 4.50
Height (cm)	171.04 ± 10.88
Weight (kg)	64.26 ± 10.27
Body-mass index (kg/m^2)	21.78 ± 2.52

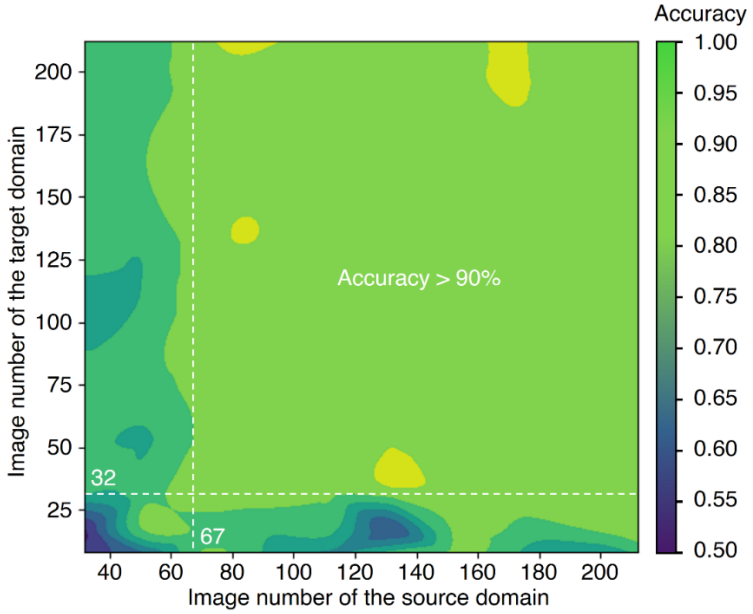

Figure 3.6: Heatmap of the classification accuracy observed after domain adaptation with different numbers of images from the target and source domains. The heatmap shows that a high accuracy (>90%) can be attained by using as few as 32 unlabeled images from the target domain and 67 labeled images from the source domain for domain adaptation training.

Acknowledgements

Chapter 3, in full, is a reprint of the material as it appears in Nature Biotechnology. Muyang Lin, Ziyang Zhang, Xiaoxiang Gao, Yizhou Bian, Ray S. Wu, Geonho Park, Zhiyuan Lou, Zhuorui Zhang, Xiangchen Xu, Xiangjun Chen, Andrea Kang, Xinyi Yang, Wentong Yue, Lu Yin, Chonghe Wang, Baiyan Qi, Sai Zhou, Hongjie Hu, Hao Huang, Mohan Li, Yue Gu, Jing Mu, Albert Yang, Amer Yaghi, Yimu Chen, Yusheng Lei, Chengchangfeng Lu, Ruotao Wang, Joseph Wang, Shu Xiang, Erik B. Kistler, Nuno Vasconcelos & Sheng Xu. "A fully integrated wearable ultrasound system to monitor deep tissues in moving subjects." Nature Biotechnology, 2023. The dissertation author was the primary investigator and author of this paper.

Chapter 4 Continuous monitoring during exercise

The USoP can continuously track multiple deep tissue signals during human motion. To test its performance, the USoP is applied on a participant while performing aerobic exercise, when the participant performed 30 min continuous cycling followed by 30 min rest. The carotid blood pressure waveform is recorded while the participant moves freely (Fig. 4.1a). Similar measurements are made during anaerobic exercise, when the participant performed high-intensity interval training (HIIT) comprised of six one-minute training sessions, separated by six one-minute periods of resting (Fig. 4.2).

Figure 4.1: Continuous monitoring during exercise. a, Photographs showing a subject cycling while the carotid pulsation waveform is measured by the USoP with different head positions, including (i) forward, (ii) turned, (iii) bowed, and (iv) raised. The USoP can directly transmit data to the smartphone mounted on the bicycle for processing and display. Inertia measurement units are used to record the head motion. An automated cuff on the upper arm acquires brachial blood pressure levels for reference. b, Head motions recorded by the inertia measurement units during cycling. The carotid blood pressure waveforms and heart rate are recorded simultaneously using the USoP. The maximum increases in diastolic and systolic pressure are 17 mmHg and 45 mmHg, respectively. c, Zoomed-in view of the head motion, blood pressure waveforms, and heart rate recorded during the (i)-(iv) motion periods in b. The diastolic carotid pressures measured by the USoP agree well with the brachial pressures measured by the cuff. The systolic carotid pressures measured by the USoP are ~10 mmHg lower than the cuff brachial values, due to lower distal reflections. d, Histograms of the diastolic and systolic pressures during cycling and HIIT. During cycling, the variations in diastolic and systolic pressures are 20 mmHg and 47 mmHg, respectively. During HIIT, the variations in diastolic and systolic pressures are 38 mmHg and 55 mmHg, respectively. e, Changes in augmentation indices during cycling and HIIT. The augmentation index first increases and then plateaus during cycling, and then recovers during resting (upper). The augmentation index fluctuates during HIIT, coinciding with the training-resting cycles (lower). Notably, the augmentation index was substantially higher during (ii) and (iv) training sessions, indicating greater arterial vasodilation. Average augmentation indices are calculated from fifty independent pulse waveforms every minute. The error bars represent the standard deviations of the recorded augmentation indices. f, Cardiac response to cycling and HIIT. In both exercise scenarios, the stroke volume first increases and then plateaus while the heart rate continues to increase. Cycling has a smaller increase in stroke volume compared to HIIT. The maximum cardiac output measured during HIIT is 15.6% greater than during cycling.

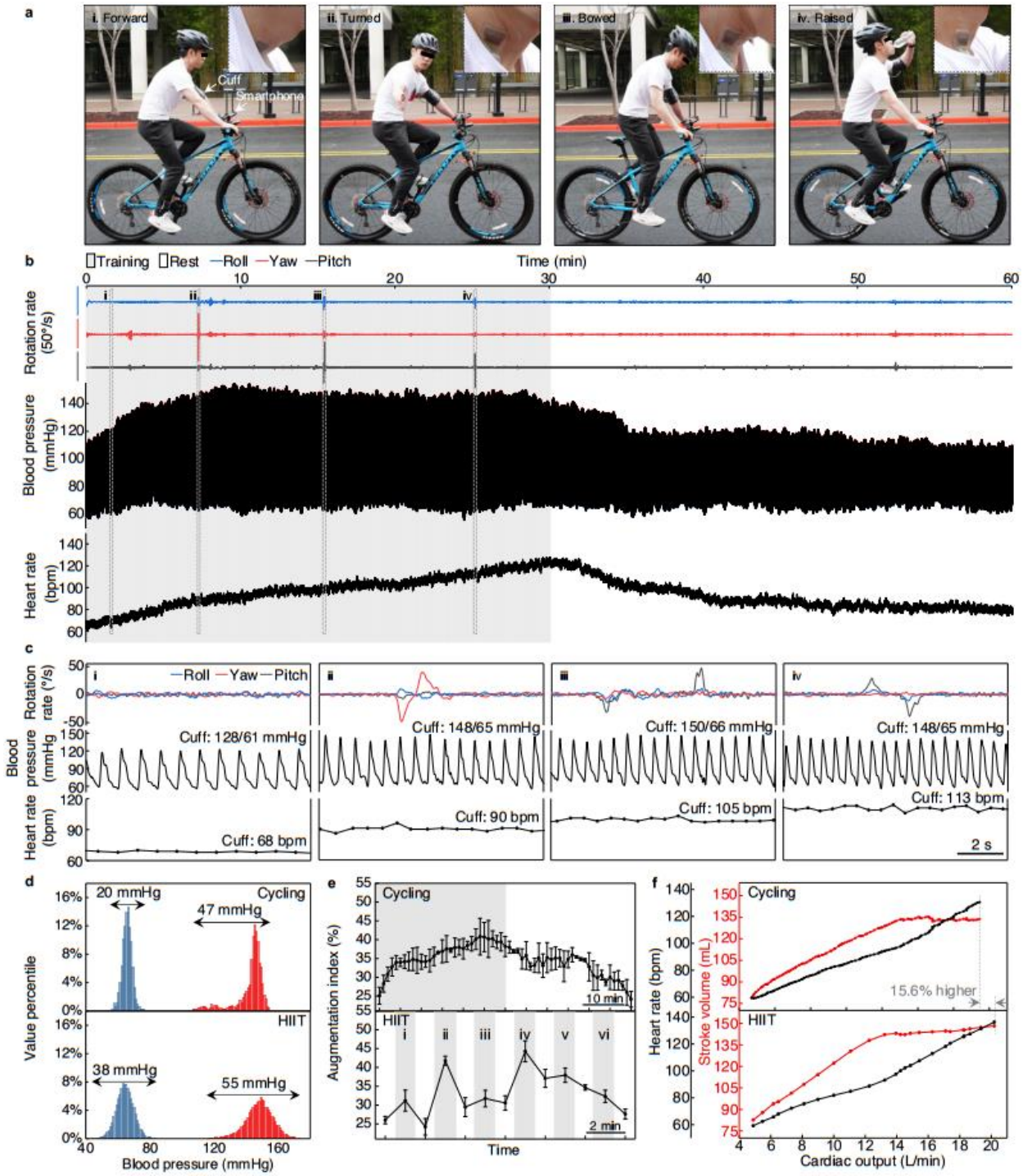
a
i. Forward
ii. Turned
iii. Bowed
iv. Raised
Cuff
Smartphone
b
Training
Rest
Roll
Yaw
Pitch
Time (min)
Rotation rate (50°/s)
Blood pressure (mmHg)
Heart rate (bpm)
c
Blood
Rotation rate (°/s)
Blood pressure (mmHg)
Heart rate (bpm)
Cuff: 128/61 mmHg
Cuff: 148/65 mmHg
Cuff: 150/66 mmHg
Cuff: 148/65 mmHg
Cuff: 68 bpm
Cuff: 90 bpm
Cuff: 105 bpm
Cuff: 113 bpm
2 s
d
Value percentile
20 mmHg
47 mmHg
38 mmHg
55 mmHg
Cycling
HIIT
Blood pressure (mmHg)
e
Augmentation index (%)
10 min
2 min
Time
f
Heart rate (bpm)
Stroke volume (mL)
15.6% higher
Cardiac output (L/min)

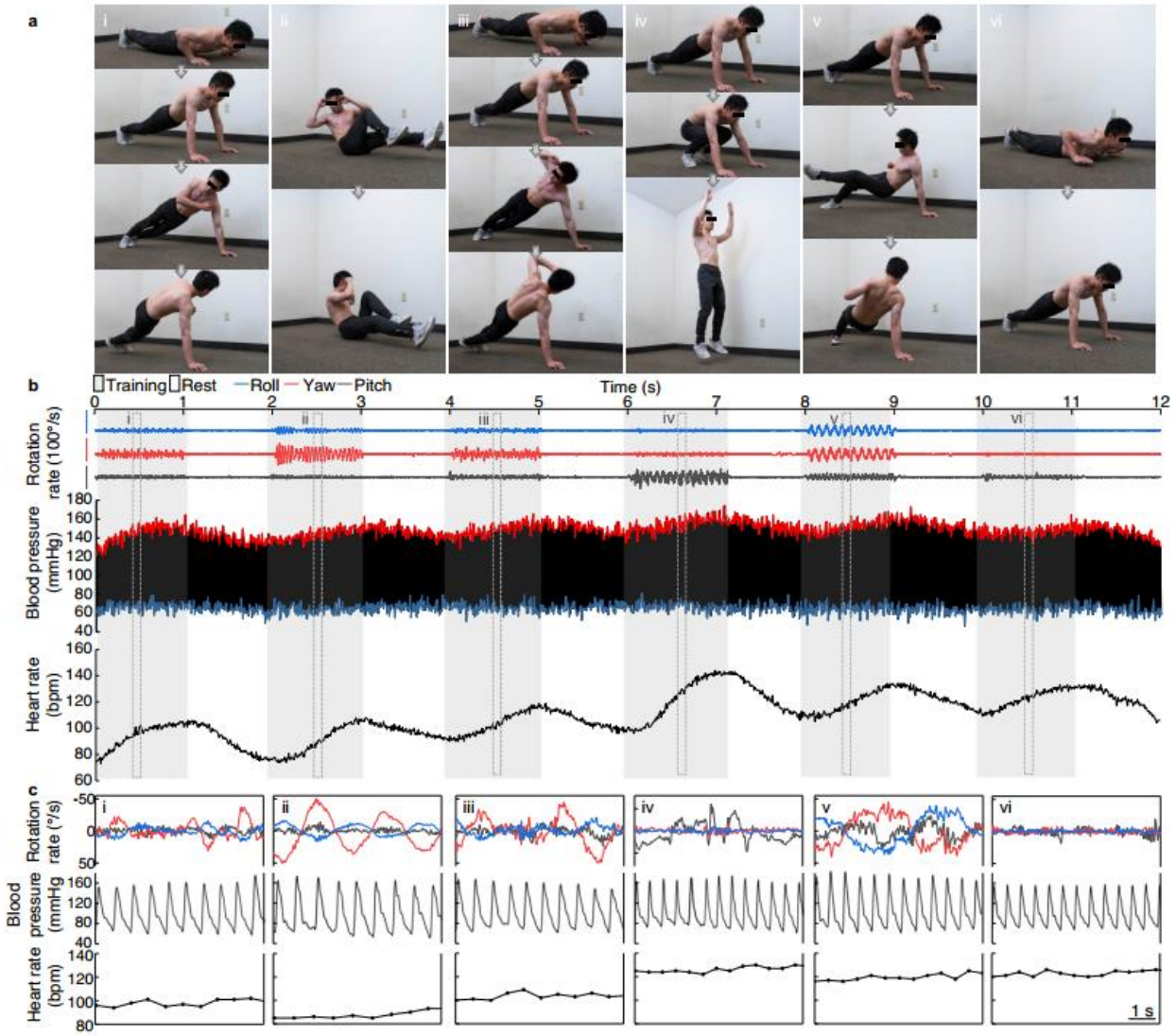

Figure 4.2: Continuous monitoring during high-intensity interval training (HIIT). a, Photographs showing the participant performing HIIT. Six training sessions, including (i) touch shoulder push-ups, (ii) cycling Russian twist, (iii) push-up rotations, (iv) burpees, (v) side kick through, and (vi) hand-release push-ups. b, The head motions are recorded by the inertia measurement units, which show the rolling, yawing, and pitching rates during the 12 min training and resting. The carotid blood pressure waveforms and heart rate are recorded simultaneously and continuously using the USoP. The systolic pressure increased ~25 mmHg between training sessions and rest sessions, while the diastolic pressure experienced less fluctuation. c, Zoomed-in view of the head motions, continuous blood pressure waveforms, and heart rate recorded during the training sessions.

Upon the onset of exercising, the substantial increase in the blood pressure and heart rate suggests a boost in circulating blood, also known as the stressed volume (Fig. 4.1b-c)[48]. During both cycling and HIIT, the systolic pressure increases more than the diastolic pressure, regulated

by increased cardiac output and decreased vascular resistance. The heart rate increases monotonically during both exercises and decreases during resting, as anticipated[49]. As cycling progresses, the blood pressure gradually stabilizes at a relatively elevated level, resulting in narrow distributions of both systolic and diastolic pressures in the histogram (Fig. 4.1d upper). These results imply that the systemic vascular resistance decreases to a physiologically determined steady state to support prolonged muscle activity[50]. This is in stark contrast to HIIT, during which blood pressure fluctuates, resulting in wider distributions of both diastolic and systolic blood pressures (Fig. 4.1d lower). In both cycling and HIIT, resting allows blood pressure to gradually decrease toward the baseline.

The vascular responses to exercise is derived by calculating the augmentation index[51,52] In both cycling and HIIT, the blood pressure waveforms have changing profiles, suggesting increased differences between the systolic peak and secondary (reflected) peak during exercise (Figs. 4.3). This change indicates a reduced reflection from the distal ends of the arterial tree due to flow-mediated vasodilation[53]. I used the pulse wave decomposition analysis method[54] to analyze the pulse profiles and quantify the vasodilation occurring in exercise. Using this method, the pulse waveforms measured from central arteries (e.g., aorta and carotid artery) are decomposed into the forward and reflection waves. The forward waves are generated by the heart, while the reflection waves are considered to be backpropagations from the distal ends of the arterial tree (Fig. 4.4a). More constrictive arteries are of higher impedance and tend to have stronger reflection waves and faster backpropagation speeds (Fig. 4.4b upper panel). This results in an early and strong reflection peak in the arterial pulse waveform. On the contrary, dilated arteries are of lower impedance, which have weaker reflections and slower backpropagation speeds, and thus, lead to a late and mild reflection peak in the pulse waveform. I used the AIx to quantify vasodilation[55]. The AIx is defined

as the difference between the systolic peak and the reflection peak/inflection point divided by the systolic peak. Example waveforms recorded before and after exercise indicate an increase in the AIx due to dilated arteries and decreased impedance of pulse wave propagation post-exercise (Fig. 4.4b lower panel). In practice, the AIx can be calculated in a beat-to-beat manner from the blood pressure waveforms. In this work, the beat-to-beat AIx's were averaged over every minute to minimize potential errors associated with accidental waveform distortions.

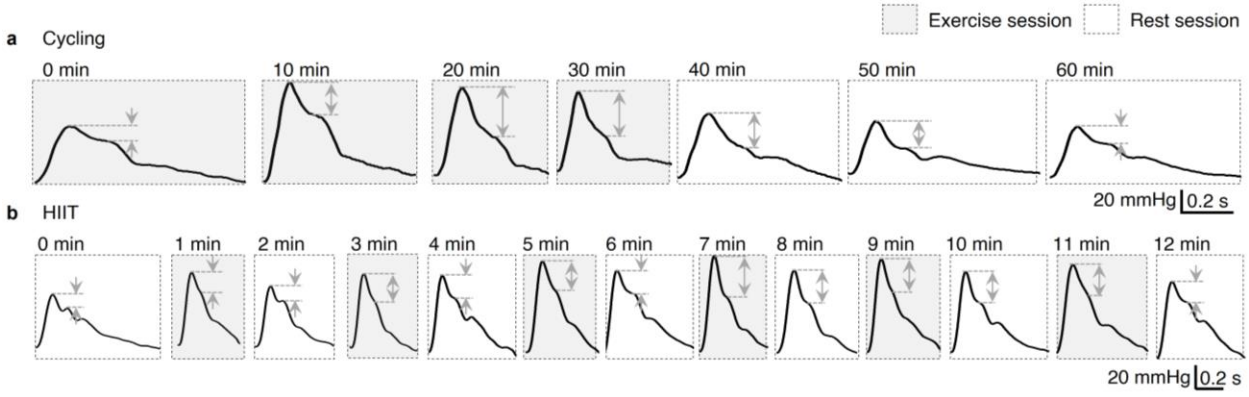

Figure 4.3: Representative pressure waveforms recorded during cycling and HIIT. Central blood pressure waveforms recorded during a, cycling and b, HIIT. The waveform morphologies change significantly during exercise sessions. In both exercise scenarios, the difference between the systolic pressure peak and reflection pressure peak increases during exercise, indicating reduced distal reflection and increased vasodilation during exercise.

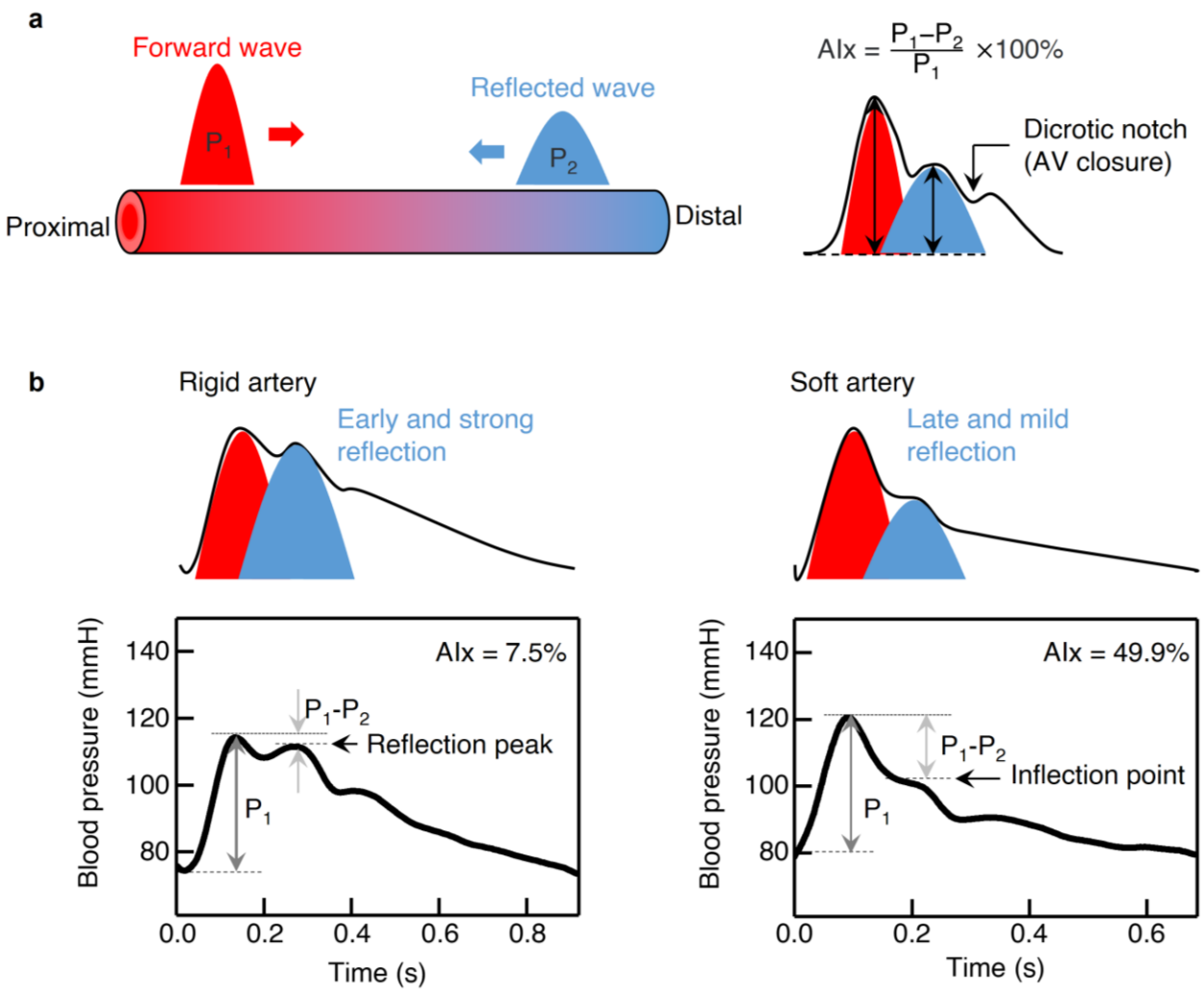

Figure 4.4: Measurements of the AIx. a, Schematics showing the arterial blood pulse waveform formation and the calculation of the AIx. The forward wave (P_1) and reflected wave (P_2) constitute local peaks in a blood pressure waveform. AIx is calculated as the peak difference divided by the forward peak. There is an additional local minimum point resulting from the closure of the aortic valve (AV). b, Blood pressure waveforms from the carotid artery under resting and post-exercise situations. In a resting situation, the distal end of the arterial tree has a higher impedance, resulting in an early and strong reflection peak P_2. On the contrary, in a post-exercise situation, the distal end has a lower impedance, resulting in a late and mild reflection peak P_2.

In both cycling and HIIT, the augmentation index increases with exercise and recovers with resting; when the exercise is sufficiently long, as in the case of cycling, the augmentation index

stabilizes (Fig. 4.1e). The increase in the augmentation index during exercise may have two causes: vessel stiffening[56] and vasodilation[52,57]. The change in the arterial stiffness index before, during, and after exercise are measured. The results suggest a negligible change (<0.34%) in the stiffness index[58]. Therefore, the increase in the augmentation index is primarily driven by vasodilation rather than changes in arterial stiffness. The vasodilation takes place mainly in the skeletal muscle involved in the exercise to support an elevated demand for oxygen and thus blood flow[52,59]; activating larger muscle groups results in greater vasodilation and increased blood flow, and thus a higher augmentation index (Fig. 4.4).

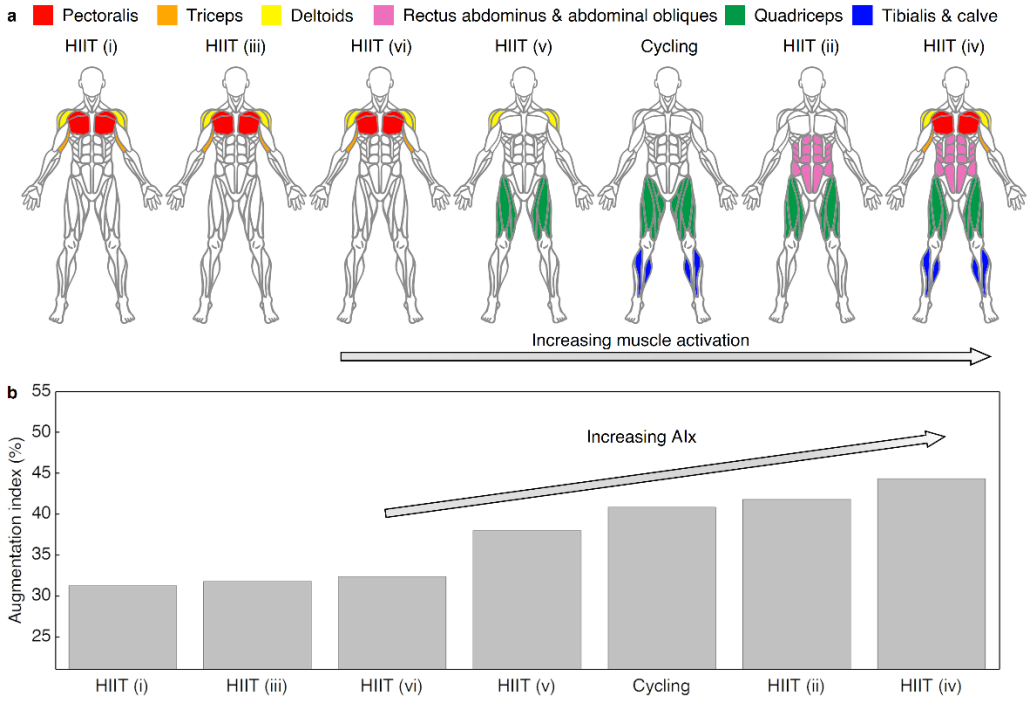

Figure 4.5: Muscle recruitments and corresponding AIx during cycling and HIIT. a, Different muscle groups are involved during cycling and HIIT. HIIT (i), (iii), and (vi) share the same least muscle activation, during which the pectoralis, deltoids, and triceps are activated. HIIT (v) has the second least muscle activation, during which the deltoids and quadriceps are activated. Cycling has more muscle activation, during which quadriceps, tibialis, and calve are activated. The HIIT (ii) has the second most muscle activation, during which the rectus abdominus, abdominal obliques, and quadriceps are activated. The HIIT (iv) has the most muscle activation, during which all muscle groups mentioned above are activated. b, The calculated AIx during exercise, which increases with increasing the amount of muscles activated during exercise.

The stroke volume could be estimated from the pressure waveforms using a pulse contour method (Fig. 4.6)[60]. In the Windkessel model of the circulation[61], the blood pressure waveform can be used to monitor fluid flow throughout the circulatory system, such as flow velocity, distensibility, pressure, and volume, which allows relating the pulse contour waveform to the stroke volume.

In the Windkessel model, the distensibility c is expressed as[61]:

$$c = \frac{dP}{dV} = c$$

where P is pressure and V is the volume of the fluid. The main differential equation describing the system is written as[61]:

$$i*dt = \frac{dP}{c} + \frac{P*dt}{w}$$

or

$$dt = \frac{dP}{c\left(i - \frac{P}{w}\right)}$$

where i is the volume of liquid flowing in per unit time; t is time; and w is the constant $\frac{8L\mu}{\pi r^4}$ from Poiseuille's law.

Because the artery is nonrigid, the inflow and outflow at a given time are not equal to each other even though the blood is an incompressible fluid. Therefore, i should be averaged over the entire cardiac cycle. Integrating the main differential equation leads to[61]:

$$t = -\left[\frac{w}{c}\left(i - \frac{P}{w}\right)\right] + \left[\frac{w}{c}\left(i - \frac{P_0}{w}\right)\right]$$

for a nonzero initial pressure P_0 at time $t = 0$. The equation then becomes[61]:

$$t = \frac{w}{c}\left(\frac{i - \frac{P_0}{w}}{i - \frac{P}{w}}\right)$$

leading to the pressure equation[61]:

$$P=w\left(i-\frac{i-\frac{P_0}{w}}{e^{\frac{t_c}{w}}}\right)$$

Wesseling and coworkers have used the aforementioned Windkessel model as a basis for calculating the stroke volume by integrating the area under the curve of the pulse contour[62,63]. In essence, the pressure increases in proximal large arteries (e.g., aorta or carotid) are determined by the systolic blood output from the heart. Therefore the area under the systolic portion is proportionally related to the stroke volume[60], by a factor representing the characteristic impedance of the circulatory system, Z[62,63]:

$$\text{Stroke Volume}=\frac{1}{Z}\int_0^{T_e}[P(t)-P_d]dt$$

where T_e is the end of the ejection period; P(t) is the real-time blood pressure; and P_d is the diastolic pressure. The characteristic impedance Z may be calibrated to another measure of stroke volume such as indicator dilution, or simply estimated using factors such as age, sex, height, and weight of the subject[63,64]. In this study, an estimated value for the participant's characteristic impedance Z=0.056 mmHg·s/ml[65] is used.

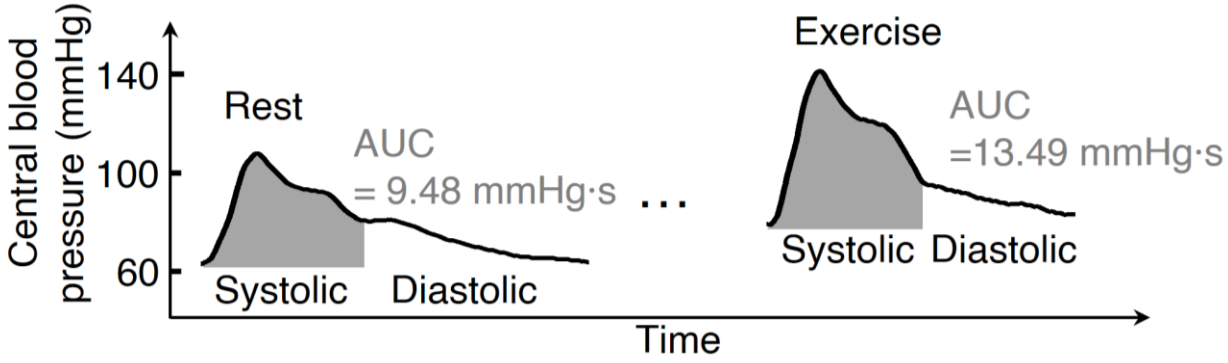

Figure 4.6: Estimation of the stroke volume by the pulse contour method. Two central blood pressure waveforms collected from the carotid artery during rest and exercise. The area under the curve (AUC) of the systolic phase is enlarged, indicating an increased stroke volume during exercise.

The cardiac output is then calculated as the product of stroke volume and heart rate. Similar patterns in the stroke volume and heart rate are observed in both cycling and HIIT (Fig. 4.1f). The measured cardiac output increases as the exercise intensifies, and the heart rate increases together with the cardiac output. Initially, the stroke volume increases before plateauing as end-systolic volume approaches the mechanical limits of the heart[66] and the increase of end-diastolic volume begins to be limited by the shorter filling times at higher heart rates[67]. In the high cardiac output region (e.g., >15 L/min), the stroke volume plateaus, and the increase in cardiac output is mainly attributed to the increase in heart rate[68]. Compared to cycling, HIIT produces a greater increase in stroke volume and a higher maximum cardiac output, indicating that HIIT may be a more effective training modality for enhancing cardiac functions[69,70].

Acknowledgements

Chapter 4, in full, is a reprint of the material as it appears in Nature Biotechnology. Muyang Lin, Ziyang Zhang, Xiaoxiang Gao, Yizhou Bian, Ray S. Wu, Geonho Park, Zhiyuan Lou, Zhuorui Zhang, Xiangchen Xu, Xiangjun Chen, Andrea Kang, Xinyi Yang, Wentong Yue, Lu Yin, Chonghe Wang, Baiyan Qi, Sai Zhou, Hongjie Hu, Hao Huang, Mohan Li, Yue Gu, Jing Mu, Albert Yang, Amer Yaghi, Yimu Chen, Yusheng Lei, Chengchangfeng Lu, Ruotao Wang, Joseph Wang, Shu Xiang, Erik B. Kistler, Nuno Vasconcelos & Sheng Xu. "A fully integrated wearable ultrasound system to monitor deep tissues in moving subjects." Nature Biotechnology, 2023. The dissertation author was the primary investigator and author of this paper.

Chapter 5 Conclusion

While most existing wearable devices capture signals on or near the skin surface[71-74], such signals are often manifestations of physiological processes in deep tissues[75]. Therefore, in many clinical applications, it is critical to monitor deep tissue signals directly. More importantly, deep tissue physiology is constantly changing. To identify potential risk factors for a disease, capture its early onset, or evaluate its progression, obtaining longitudinal data over the course of days, weeks, or even months is key. This calls for a tool that enables long-term deep tissue surveillance, processes the data stream in real time, and remains accurate during human motion.

Medical ultrasound is one of the most widely used methods for deep tissue sensing, but due to the complex equipment and the requirement for an operator, traditional ultrasound exams offer point-in-time measurements only. In fact, one of the barriers that prevents traditional ultrasound from long-term use is its operator dependency[76,77]. Even with standardized exam procedures, results reported using conventional ultrasonography strongly depend on operator skill. When mishandled, manual ultrasonography may generate compromised or even erroneous results.

Recent advances in wearable ultrasonography have shown the promise of capturing deep tissue signals over the long term. Soft wearable ultrasonic probes[19,20], as well as rigid ultrasound chips integrated with soft adhesives[21], have demonstrated hands-free ultrasound signal acquisition. However, removing the requirement to handhold the probe is only the initial step toward continuous operation, and three further technical barriers remain. First, these probes have to be wired to a central processing station, which largely limits the wearing subject's mobility. Second, existing wearable ultrasound devices face challenges with measurement continuity and reliability

in moving subjects, because the device on the skin shifts in position relative to the target tissue. Third, wearables generate new challenges for manual data processing because any clinicians will be overwhelmed by the continuous data stream.

The fully integrated USoP addresses these three barriers and makes continuous surveillance of deep tissue signals possible. First, the USoP eliminates wire connections by connecting the device and the backend processing system wirelessly, which allows for large-range subject mobility. Second, the USoP uses machine learning-based algorithms to automate the data acquisition and channel selection in real time. To my knowledge, no previously reported wearable device can autonomously track a moving target. Third, deep learning-enabled data post-processing relieves the human burden and enables potential scale-up. Together, these innovations open up many new possibilities. For example, patients can be monitored as they conduct their natural daily activities, which can provide rich information that is more clinically relevant[78]. Responses to high-risk activities such as during an intense workout can be captured for more rigorous diagnostics[79,80]. Continuous monitoring over days or weeks of the dynamic changes of the cardiovascular system in response to stressors can benefit a broad range of populations, from athletes who need training optimization, to cardiac rehabilitation patients who require safety measures, and to general high-risk populations for cardiovascular risk stratification and prediction.

Future developments of this technology can be focused on the following areas. First, the soft ultrasonic probes face challenges of unknown transducer locations when conformed to dynamic and curvilinear skin surfaces. A-mode and M-mode using single transducers without beamforming are not affected, but unknown transducer locations cause phase aberration and

compromised beamforming for B-mode imaging. Potential solutions include applying additional shape sensors to map the transducer locations in real-time[81], or developing iterative contrast optimization algorithms to compensate the phase distortion of a deformed array[82]. Second, the long-term wearability of the USoP should be further improved. Integrating highly integrated chips with multilayered soft circuitry[83] could further enhance the mechanical compliance of the system. Combining wearable power harvesting devices[84] could extend the battery life of the USoP. Replacing silicone adhesives with more durable and permeable adhesives could help enhance skin integration under skin deformation and perspiration[85]. Third, the USoP can potentially be applied to other tissue targets, particularly in high-risk populations where continuous monitoring is critical. Fourth, the cloud computing resources necessary for machine learning processing limit their accessibility in remote and undeveloped regions. On-board data analytics based on power-performance balance optimization and artificial intelligence-on-a-chip technology may be a possibility[86]. Finally, through strategically tuning the ultrasound controlling parameters such as activation frequency and pulse profile, this technology could enable more intriguing wearable diagnostic and therapeutic applications, including anatomic imaging[21], functional imaging[20,87,88], and ultrasound stimulation[89].

Acknowledgements

Chapter 5, in part, is a reprint of the material as it appears in Nature Biotechnology. Muyang Lin, Ziyang Zhang, Xiaoxiang Gao, Yizhou Bian, Ray S. Wu, Geonho Park, Zhiyuan Lou, Zhuorui Zhang, Xiangchen Xu, Xiangjun Chen, Andrea Kang, Xinyi Yang, Wentong Yue, Lu Yin, Chonghe Wang, Baiyan Qi, Sai Zhou, Hongjie Hu, Hao Huang, Mohan Li, Yue Gu, Jing Mu, Albert Yang, Amer Yaghi, Yimu Chen, Yusheng Lei, Chengchangfeng Lu, Ruotao Wang, Joseph Wang, Shu Xiang, Erik B. Kistler, Nuno Vasconcelos & Sheng Xu. "A fully integrated wearable ultrasound system to monitor deep tissues in moving subjects." Nature Biotechnology, 2023. The dissertation author was the primary investigator and author of this paper.

REFERENCES

1 Savoia, A. S., Caliano, G. & Pappalardo, M. A CMUT probe for medical ultrasonography: From microfabrication to system integration. *IEEE Trans. Ultrason. Ferroelectr. Freq. Control* **59**, 1127-1138 (2012).

2 Shung, K. K., Cannata, J. & Zhou, Q. Piezoelectric materials for high frequency medical imaging applications: A review. *J. Electroceram.* **19**, 141-147 (2007).

3 Rothberg, J. M., Ralston, T. S., Rothberg, A. G., Martin, J., Zahorian, J. S., Alie, S. A., Sanchez, N. J., Chen, K., Chen, C. & Thiele, K. Ultrasound-on-chip platform for medical imaging, analysis, and collective intelligence. *Proc. Natl. Acad. Sci.* **118** (2021).

4 Brattain, L. J., Telfer, B. A., Dhyani, M., Grajo, J. R. & Samir, A. E. Machine learning for medical ultrasound: status, methods, and future opportunities. *Abdom. Radiol.* **43**, 786-799 (2018).

5 Liu, S., Wang, Y., Yang, X., Lei, B., Liu, L., Li, S. X., Ni, D. & Wang, T. Deep learning in medical ultrasound analysis: a review. *Engineering* **5**, 261-275 (2019).

6 https://www.sciencedirect.com/topics/medicine-and-dentistry/medical-ultrasonography

7 Powers, J. & Kremkau, F. Medical ultrasound systems. *Interface focus* **1**, 477-489 (2011).

8 Moran, C. M. & Thomson, A. J. Preclinical ultrasound imaging—a review of techniques and imaging applications. *Front. Phys.* **8**, 124 (2020).

9 Jensen, J. A. Medical ultrasound imaging. *Prog. Biophys. Mol. Biol.* **93**, 153-165 (2007).

10 Price, D., Wallbridge, D. & Stewart, M. Tissue Doppler imaging: current and potential clinical applications. *Heart* **84**, ii11-ii18 (2000).

11 Sigrist, R. M., Liau, J., El Kaffas, A., Chammas, M. C. & Willmann, J. K. Ultrasound elastography: review of techniques and clinical applications. *Theranostics* **7**, 1303 (2017).

12 Poelma, C. Ultrasound imaging velocimetry: a review. *Exp. Fluids* **58**, 1-28 (2017).

13 Kasban, H., El-Bendary, M. & Salama, D. A comparative study of medical imaging techniques. *Int. J. Inf. Sci. Intell. Syst.* **4**, 37-58 (2015).

14 Kalender, W. A. X-ray computed tomography. *Phys. Med. Biol.* **51**, R29 (2006).

15 Katti, G., Ara, S. A. & Shireen, A. Magnetic resonance imaging (MRI)–A review. *Int. j. dent. clin.* **3**, 65-70 (2011).

16 Díaz-Gómez, J. L., Mayo, P. H. & Koenig, S. J. Point-of-Care Ultrasonography. *N. Engl. J. Med.* **385**, 1593-1602 (2021).

17 Kenny, J.-É. S., Munding, C. E., Eibl, J. K., Eibl, A. M., Long, B. F., Boyes, A., Yin, J., Verrecchia, P., Parrotta, M. & Gatzke, R. A novel, hands-free ultrasound patch for continuous monitoring of quantitative Doppler in the carotid artery. *Sci. Rep.* **11**, 1-11 (2021).

18 Hu, H., Zhu, X., Wang, C., Zhang, L., Li, X., Lee, S., Huang, Z., Chen, R., Chen, Z. & Wang, C. Stretchable ultrasonic transducer arrays for three-dimensional imaging on complex surfaces. *Sci. Adv.* **4**, eaar3979 (2018).

19 Wang, C., Li, X., Hu, H., Zhang, L., Huang, Z., Lin, M., Zhang, Z., Yin, Z., Huang, B. & Gong, H. Monitoring of the central blood pressure waveform via a conformal ultrasonic device. *Nat. Biomed. Eng.* **2**, 687-695 (2018).

20 Wang, C., Qi, B., Lin, M., Zhang, Z., Makihata, M., Liu, B., Zhou, S., Huang, Y.-h., Hu, H. & Gu, Y. Continuous monitoring of deep-tissue haemodynamics with stretchable ultrasonic phased arrays. *Nat. Biomed. Eng.* **5**, 749-758, doi:https://doi.org/10.1038/s41551-021-00763-4 (2021).

21 Wang, C., Chen, X., Wang, L., Makihata, M., Liu, H.-C., Zhou, T. & Zhao, X. Bioadhesive ultrasound for long-term continuous imaging of diverse organs. *Science* **377**, 517-523, doi:10.1126/science.abo2542 (2022).

22 https://pulsify-medical.com/.

23 https://penta-eureka.eu/wp-content/uploads/2022/02/Penta_Project-Ulimpia_Impact_Summary-18_11_2021.pdf.

24 Baribeau, Y., Sharkey, A., Chaudhary, O., Krumm, S., Fatima, H., Mahmood, F. & Matyal, R. Handheld point-of-care ultrasound probes: the new generation of POCUS. *J. Cardiothorac. Vasc. Anesth.* **34**, 3139-3145 (2020).

25 Hu, H., Huang, H., Li, M., Gao, X., Yin, L., Qi, R., Wu, R. S., Chen, X., Ma, Y., Shi, K., Li, C., Maus, T. M., Huang, B., Lu, C., Lin, M., Zhou, S., Lou, Z., Gu, Y., Chen, Y., Lei, Y., Wang, X., Wang, R., Yue, W., Yang, X., Bian, Y., Mu, J., Park, G., Xiang, S., Cai, S., Corey, P. W., Wang, J. & Xu, S. A wearable cardiac ultrasound imager. *Nature* **613**, 667-675, doi:10.1038/s41586-022-05498-z (2023).

26 https://standards.ieee.org/ieee/802.11/5536/.

27 Carovac, A., Smajlovic, F. & Junuzovic, D. Application of ultrasound in medicine. *Acta Inform. Med.* **19**, 168 (2011).

28 Feigenbaum, H. Role of M-mode technique in today's echocardiography. *J. Am. Soc. Echocardiogr.* **23**, 240-257 (2010).

29 Gamble, G., Zorn, J., Sanders, G., MacMahon, S. & Sharpe, N. Estimation of arterial stiffness, compliance, and distensibility from M-mode ultrasound measurements of the common carotid artery. *Stroke* **25**, 11-16 (1994).

30 Testa, A., Soldati, G., Giannuzzi, R., Berardi, S., Portale, G. & Silveri, N. G. Ultrasound M-mode assessment of diaphragmatic kinetics by anterior transverse scanning in healthy subjects. *Ultrasound Med. Biol.* **37**, 44-52 (2011).

31 Prada, G., Vieillard-Baron, A., Martin, A. K., Hernandez, A., Mookadam, F., Ramakrishna, H. & Diaz-Gomez, J. L. Echocardiographic applications of M-mode ultrasonography in anesthesiology and critical care. *J. Cardiothorac. Vasc. Anesth.* **33**, 1559-1583 (2019).

32 Hayashi, K., Handa, H., Nagasawa, S., Okumura, A. & Moritake, K. Stiffness and elastic behavior of human intracranial and extracranial arteries. *J. Biomech.* **13**, 175-184 (1980).

33 Bonarjee, V. V. Arterial stiffness: a prognostic marker in coronary heart disease. available methods and clinical application. *Front. Cardiovasc. Med.* **5**, 64 (2018).

34 Uejima, T., Dunstan, F. D., Arbustini, E., Łoboz-Grudzień, K., Hughes, A. D., Carerj, S., Favalli, V., Antonini-Canterin, F., Vriz, O. & Vinereanu, D. Age-specific reference values for carotid arterial stiffness estimated by ultrasonic wall tracking. *J. Hum. Hypertens.* **34**, 214-222 (2020).

35 Meinders, J. M. & Hoeks, A. P. Simultaneous assessment of diameter and pressure waveforms in the carotid artery. *Ultrasound Med. Biol.* **30**, 147-154 (2004).

36 Palombo, C. & Kozakova, M. Arterial stiffness, atherosclerosis and cardiovascular risk: Pathophysiologic mechanisms and emerging clinical indications. *Vasc. Pharmacol.* **77**, 1-7 (2016).

37 Bourgeois, B., Watts, K., Thomas, D. M., Carmichael, O., Hu, F. B., Heo, M., Hall, J. E. & Heymsfield, S. B. Associations between height and blood pressure in the United States population. *Medicine (Baltimore)* **96** (2017).

38 Sleight, P. Lowering of blood pressure and artery stiffness. *The Lancet* **349**, 955-956 (1997).

39 Witteman, J. C., Grobbee, D. E., Valkenburg, H. A., Stijnen, T., Burger, H., Hofman, A. & van Hemert, A. J-shaped relation between change in diastolic blood pressure and progression of aortic atherosclerosis. *The Lancet* **343**, 504-507 (1994).

40 Evans, J. M., Wang, S., Greb, C., Kostas, V., Knapp, C. F., Zhang, Q., Roemmele, E. S., Stenger, M. B. & Randall, D. C. Body size predicts cardiac and vascular resistance effects on men's and women's blood pressure. *Front. Physiol.* **8**, 561 (2017).

41 Grensemann, J. Cardiac output monitoring by pulse contour analysis, the technical basics of less-invasive techniques. *Front. Med.* **5**, 64 (2018).

42 Stabouli, S., Printza, N., Zervas, C., Dotis, J., Chrysaidou, K., Maliahova, O., Antza, C., Papachristou, F. & Kotsis, V. Comparison of the SphygmoCor XCEL device with

applanation tonometry for pulse wave velocity and central blood pressure assessment in youth. *J. Hypertens.* **37**, 30-36 (2019).

43 Elliot, C. A., Hamlin, M. J. & Lizamore, C. A. Inter-operator Reliability for Measuring Pulse Wave Velocity and Augmentation Index. *Front. Cardiovasc. Med.* **7**, 72 (2020).

44 Hoesein, F. A. M., Zanen, P. & Lammers, J.-W. J. Lower limit of normal or FEV1/FVC< 0.70 in diagnosing COPD: an evidence-based review. *Respir. Med.* **105**, 907-915 (2011).

45 Johnson, J. D. & Theurer, W. M. A stepwise approach to the interpretation of pulmonary function tests. *Am. Fam. Physician* **89**, 359-366 (2014).

46 Limbu, Y. R., Gurung, G., Malla, R., Rajbhandari, R. & Regmi, S. R. Assessment of carotid artery dimensions by ultrasound in non-smoker healthy adults of both sexes. *Nepal Med Coll J* **8**, 200-203 (2006).

47 Morerio, P., Cavazza, J. & Murino, V. in *International Conference on Learning Representations* (2018).

48 Magder, S. Volume and its relationship to cardiac output and venous return. *Crit. Care* **20**, 1-11 (2016).

49 White, D. W. & Raven, P. B. Autonomic neural control of heart rate during dynamic exercise: revisited. *J. Physiol.* **592**, 2491-2500 (2014).

50 Laughlin, M. H., Korthuis, R. J., Duncker, D. J. & Bache, R. J. Control of blood flow to cardiac and skeletal muscle during exercise. *Compr. Physiol.*, 705-769 (2010).

51 O'Rourke, M. F. & Mancia, G. Arterial stiffness. *J. Hypertens.* **17**, 1-4 (1999).

52 Plowman, S. A. & Smith, D. L. *Exercise physiology for health fitness and performance*. (Lippincott Williams & Wilkins, 2013).

53 Weissgerber, T. L. Flow-Mediated Dilation: Can New Approaches Provide Greater Mechanistic Insight into Vascular Dysfunction in Preeclampsia and Other Diseases? *Curr. Hypertens. Rep.* **16**, 1-10 (2014).

54 Baruch, M. C., Kalantari, K., Gerdt, D. W. & Adkins, C. M. Validation of the pulse decomposition analysis algorithm using central arterial blood pressure. *Biomed. Eng. Online* **13**, 1-19 (2014).

55 Laurent, S., Cockcroft, J., Van Bortel, L., Boutouyrie, P., Giannattasio, C., Hayoz, D., Pannier, B., Vlachopoulos, C., Wilkinson, I. & Struijker-Boudier, H. Expert consensus document on arterial stiffness: methodological issues and clinical applications. *Eur. Heart J.* **27**, 2588-2605 (2006).

56 Salvi, P. in *Pulse Waves* 19-68 (Springer, 2017).

57 Munir, S., Jiang, B., Guilcher, A., Brett, S., Redwood, S., Marber, M. & Chowienczyk, P. Exercise reduces arterial pressure augmentation through vasodilation of muscular arteries in humans. *Am. J. Physiol. Heart Circ. Physiol.* **294**, H1645-H1650 (2008).

58 Antonini-Canterin, F., Carerj, S., Di Bello, V., Di Salvo, G., La Carrubba, S., Vriz, O., Pavan, D., Balbarini, A. & Nicolosi, G. L. Arterial stiffness and ventricular stiffness: a couple of diseases or a coupling disease? A review from the cardiologist's point of view. *Eur. J. Echocardiogr.* **10**, 36-43 (2008).

59 Brett, S. E., Ritter, J. M. & Chowienczyk, P. J. Diastolic blood pressure changes during exercise positively correlate with serum cholesterol and insulin resistance. *Circulation* **101**, 611-615 (2000).

60 Scolletta, S., Biagioli, B. & Giomarelli, P. in *Anaesthesia, Pain, Intensive Care and Emergency APICE* 225-236 (Springer, 2007).

61 Frank, O. The basic shape of the arterial pulse. First treatise: mathematical analysis. *J. Mol. Cell. Cardiol.* **22**, 255-277 (1990).

62 Wesseling, K. A simple device for the continuous measurement of cardiac output. Its model basis and experimental varification. *Adv. Cardiovasc. Phys.* **5**, 16-52 (1983).

63 Wesseling, K., Jansen, J., Settels, J. & Schreuder, J. Computation of aortic flow from pressure in humans using a nonlinear, three-element model. *J. Appl. Physiol.* **74**, 2566-2573 (1993).

64 Kobe, J., Mishra, N., Arya, V. K., Al-Moustadi, W., Nates, W. & Kumar, B. Cardiac output monitoring: Technology and choice. *Ann. Card. Anaesth.* **22**, 6 (2019).

65 Bikia, V., Rovas, G., Pagoulatou, S. & Stergiopulos, N. Determination of Aortic Characteristic Impedance and Total Arterial Compliance From Regional Pulse Wave Velocities Using Machine Learning: An in-silico Study. *Front. Bioeng. Biotechnol.* **9**, 345 (2021).

66 Stöhr, E. J., González-Alonso, J. & Shave, R. Left ventricular mechanical limitations to stroke volume in healthy humans during incremental exercise. *Am. J. Physiol. Heart Circ. Physiol.* **301**, H478-H487 (2011).

67 Vieira, S. S., Lemes, B., de Carvalho, P. d. T., de Lima, R. N., Bocalini, D. S., Junior, J. A., Arsa, G., Casarin, C. A., Andrade, E. L. & Serra, A. J. Does stroke volume increase during an incremental exercise? A systematic review. *The Open Cardiovascular Medicine Journal* **10**, 57 (2016).

68 Glynn, A. J. & Fiddler, H. *The Physiotherapist's Pocket Guide to Exercise E-Book: Assessment, Prescription and Training*. (Elsevier Health Sciences, 2009).

69 Guiraud, T., Nigam, A., Gremeaux, V., Meyer, P., Juneau, M. & Bosquet, L. High-intensity interval training in cardiac rehabilitation. *Sports Med.* **42**, 587-605 (2012).

70 Hannan, A. L., Hing, W., Simas, V., Climstein, M., Coombes, J. S., Jayasinghe, R., Byrnes, J. & Furness, J. High-intensity interval training versus moderate-intensity continuous training within cardiac rehabilitation: a systematic review and meta-analysis. *Open Access J. Sports Med.* **9**, 1 (2018).

71 Gao, W., Emaminejad, S., Nyein, H. Y. Y., Challa, S., Chen, K., Peck, A., Fahad, H. M., Ota, H., Shiraki, H. & Kiriya, D. Fully integrated wearable sensor arrays for multiplexed in situ perspiration analysis. *Nature* **529**, 509 (2016).

72 Kim, J., Salvatore, G. A., Araki, H., Chiarelli, A. M., Xie, Z., Banks, A., Sheng, X., Liu, Y., Lee, J. W. & Jang, K.-I. Battery-free, stretchable optoelectronic systems for wireless optical characterization of the skin. *Sci. Adv.* **2**, e1600418 (2016).

73 Huang, X., Liu, Y., Cheng, H., Shin, W. J., Fan, J. A., Liu, Z., Lu, C. J., Kong, G. W., Chen, K. & Patnaik, D. Materials and designs for wireless epidermal sensors of hydration and strain. *Adv. Funct. Mater.* **24**, 3846-3854 (2014).

74 Kim, J., Gutruf, P., Chiarelli, A. M., Heo, S. Y., Cho, K., Xie, Z., Banks, A., Han, S., Jang, K. I. & Lee, J. W. Miniaturized Battery-Free Wireless Systems for Wearable Pulse Oximetry. *Adv. Funct. Mater.* **27** (2017).

75 Lin, M., Hu, H., Zhou, S. & Xu, S. Soft wearable devices for deep-tissue sensing. *Nat. Rev. Mater.* **7**, 850–869, doi:10.1038/s41578-022-00427-y (2022).

76 Naqvi, J., Yap, K. H., Ahmad, G. & Ghosh, J. Transcranial Doppler ultrasound: a review of the physical principles and major applications in critical care. *International journal of vascular medicine* **2013** (2013).

77 Koski, J. M., Saarakkala, S., Helle, M., Hakulinen, U., Heikkinen, J. O., Hermunen, H., Balint, P., Bruyn, G. A., Filippucci, E. & Grassi, W. Assessing the intra-and inter-reader reliability of dynamic ultrasound images in power Doppler ultrasonography. *Ann. Rheum. Dis.* **65**, 1658-1660 (2006).

78 Banegas, J. R., Segura, J. n., Sobrino, J., Rodríguez-Artalejo, F., De La Sierra, A., de la Cruz, J. J., Gorostidi, M., Sarría, A. & Ruilope, L. M. Effectiveness of blood pressure control outside the medical setting. *Hypertension* **49**, 62-68 (2007).

79 Cosson, E., Paycha, F., Paries, J., Cattan, S., Ramadan, A., Meddah, D., Attali, J.-R. & Valensi, P. Detecting silent coronary stenoses and stratifying cardiac risk in patients with diabetes: ECG stress test or exercise myocardial scintigraphy? *Diabet. Med.* **21**, 342-348, doi:https://doi.org/10.1111/j.1464-5491.2004.01157.x (2004).

80 Miyai, N., Arita, M., Miyashita, K., Morioka, I., Shiraishi, T. & Nishio, I. Blood pressure response to heart rate during exercise test and risk of future hypertension. *Hypertension* **39**, 761-766 (2002).

81 Lane, C. J. The inspection of curved components using flexible ultrasonic arrays and shape sensing fibres. *Case Stud. Nondestr.Test. Eval.* **1**, 13-18 (2014).

82 Hunter, A. J., Drinkwater, B. W. & Wilcox, P. D. Autofocusing ultrasonic imagery for non-destructive testing and evaluation of specimens with complicated geometries. *Ndt & E International* **43**, 78-85 (2010).

83 Huang, Z., Hao, Y., Li, Y., Hu, H., Wang, C., Nomoto, A., Pan, T., Gu, Y., Chen, Y. & Zhang, T. Three-dimensional integrated stretchable electronics. *Nat. Electron.* **1**, 473-480 (2018).

84 Yin, L., Kim, K. N., Lv, J., Tehrani, F., Lin, M., Lin, Z., Moon, J.-M., Ma, J., Yu, J. & Xu, S. A self-sustainable wearable multi-modular E-textile bioenergy microgrid system. *Nat. Commun.* **12**, 1-12 (2021).

85 Baik, S., Lee, H. J., Kim, D. W., Kim, J. W., Lee, Y. & Pang, C. Bioinspired adhesive architectures: from skin patch to integrated bioelectronics. *Adv. Mater.* **31**, 1803309 (2019).

86 Isozaki, A., Harmon, J., Zhou, Y., Li, S., Nakagawa, Y., Hayashi, M., Mikami, H., Lei, C. & Goda, K. AI on a chip. *Lab Chip* **20**, 3074-3090 (2020).

87 Gao, X., Chen, X., Hu, H., Wang, X., Mu, J., Lou, Z., Zhang, R., Shi, K., Yue, W. & Chen, X. A photoacoustic patch for three-dimensional imaging of hemoglobin and core temperature. (2021).

88 Wang, F., Jin, P., Feng, Y., Fu, J., Wang, P., Liu, X., Zhang, Y., Ma, Y., Yang, Y., Yang, A. & Feng, X. Flexible Doppler ultrasound device for the monitoring of blood flow velocity. *Sci. Adv.* **7**, eabi9283, doi:doi:10.1126/sciadv.abi9283 (2021).

89 Li, S., Xu, J., Li, R., Wang, Y., Zhang, M., Li, J., Yin, S., Liu, G., Zhang, L., Li, B., Gu, Q. & Su, Y. Stretchable Electronic Facial Masks for Sonophoresis. *ACS Nano* **16**, 5961-5974, doi:10.1021/acsnano.1c11181 (2022).